

The C-Band All-Sky Survey (C-BASS): constraining diffuse Galactic radio emission in the North Celestial Pole region

C. Dickinson , 1,2 A. Barr, H. C. Chiang, 3,4 C. Copley, 5,6,7 R. D. P. Grumitt, S. E. Harper, H. M. Heilgendorff, L. R. P. Jew, J. L. Jonas, Michael E. Jones, J. P. Leahy, J. Leech, E. M. Leitch, S. J. C. Muchovej, T. J. Pearson, M. W. Peel, A. C. S. Readhead, J. Sievers, M. A. Stevenson and Angela C. Taylor

Accepted 2019 February 17. Received 2019 February 15; in original form 2018 October 27

ABSTRACT

The C-Band All-Sky Survey (C-BASS) is a high sensitivity all-sky radio survey at an angular resolution of 45 arcmin and a frequency of 4.7 GHz. We present a total intensity map of the North Celestial Pole (NCP) region of sky, above declination >+80°, which is limited by source confusion at a level of ≈0.6 mK rms. We apply the template-fitting (cross-correlation) technique to WMAP and Planck data, using the C-BASS map as the synchrotron template, to investigate the contribution of diffuse foreground emission at frequencies ~20–40 GHz. We quantify the anomalous microwave emission (AME) that is correlated with far-infrared dust emission. The AME amplitude does not change significantly (<10 per cent) when using the higher frequency C-BASS 4.7 GHz template instead of the traditional Haslam 408 MHz map as a tracer of synchrotron radiation. We measure template coefficients of 9.93 ± 0.35 and 9.52 ± 0.34 K per unit τ_{353} when using the Haslam and C-BASS synchrotron templates, respectively. The AME contributes $55 \pm 2 \,\mu\text{K}$ rms at 22.8 GHz and accounts for ≈ 60 per cent of the total foreground emission. Our results show that a harder (flatter spectrum) component of synchrotron emission is not dominant at frequencies \gtrsim 5 GHz; the best-fitting synchrotron temperature spectral index is $\beta = -2.91 \pm 0.04$ from 4.7 to 22.8 GHz and $\beta = -2.85 \pm 0.14$ from 22.8 to 44.1 GHz. Free-free emission is weak, contributing \approx 7 μK rms (\approx 7 per cent) at 22.8 GHz. The best explanation for the AME is still electric dipole emission from small spinning dust grains.

Key words: radiation mechanisms: non-thermal – radiation mechanisms: thermal – surveys – diffuse radiation – radio continuum: ISM.

1 INTRODUCTION

Diffuse radio foreground emission is a useful tool for studying the various components of the interstellar medium (ISM), including cosmic ray electrons via synchrotron radiation (Lawson et al. 1987; Strong, Orlando & Jaffe 2011; Orlando & Strong 2013) and warm ionized medium (WIM) via free–free emission (Davies et al. 2006; Jaffe et al. 2011; Planck Collaboration XXI 2011a; Alves et al. 2012). Understanding their detailed spatial and spectral characteristics is also important for removing them from

¹Jodrell Bank Centre for Astrophysics, Alan Turing Building, School of Physics and Astronomy, The University of Manchester, Oxford Road, Manchester, M13 9PL Manchester, UK

²Cahill Centre for Astronomy and Astrophysics, California Institute of Technology, Pasadena, CA 91125, USA

³Department of Physics, McGill University, 3600 Rue University, Montréal, QC H3A 2T8, Canada

⁴Astrophysics & Cosmology Research Unit, School of Mathematics, Statistics & Computer Science, University of KwaZulu-Natal, Westville Campus, Private Bag X54001, Durban 4000, South Africa

⁵Department of Physics and Electronics, Rhodes University, Grahamstown 6139, South Africa

⁶South African Radio Astronomy Observatory, 2 Fir Road, Observatory, Cape Town 7925, South Africa

⁷Sub-department of Astrophysics, University of Oxford, Denys Wilkinson Building, Keble Road, Oxford OX1 3RH, UK

⁸Departamento de Física Matematica, Instituto de Física, Universidade de São Paulo, Rua do Matão 1371, São Paulo, Brazil

⁹School of Chemistry and Physics, University of KwaZulu-Natal, Westville Campus, Private Bag X54001, Durban 4000, South Africa

^{*} E-mail: Clive.Dickinson@manchester.ac.uk

cosmic microwave background (CMB) data (Leach et al. 2008; Delabrouille & Cardoso 2009; Dunkley et al. 2009a; Armitage-Caplan et al. 2012; Errard & Stompor 2012; Planck Collaboration XII, IV 2013a, 2016b; Remazeilles et al. 2016).

An additional component, referred to as anomalous microwave emission (AME), has been detected at frequencies ~10-60 GHz (Kogut et al. 1996; Leitch et al. 1997; Banday et al. 2003; Lagache 2003; de Oliveira-Costa et al. 2004; Davies et al. 2006; Gold et al. 2011; Kogut et al. 2011; Ghosh et al. 2012); see Dickinson et al. (2018) for a recent review. This emission does not appear to correlate with low radio frequency data, such as the 408 MHz map by Haslam et al. (1982), which rules out steep-spectrum synchrotron emission as a cause. Similarly, analyses have shown that AME does not strongly correlate with H α data (e.g. Dickinson, Davies & Davis 2003; Finkbeiner 2003), which rules out free-free emission from warm ($T_e \approx 10^4 \text{ K}$) ionized gas. However, AME is remarkably wellcorrelated with far-infrared (FIR) and sub-mm maps (Leitch et al. 1997; Miville-Deschênes & Lagache 2005) which trace interstellar dust grains in the ISM. Draine & Lazarian (1998a) revisited the theory of electric dipole radiation from small spinning dust grains ('spinning dust'), originally postulated by Erickson (1957), and showed that spinning dust can naturally account for AME and explain the close correlation with FIR emission. Since then, there has been considerable evidence for spinning dust emission from molecular clouds and H II regions (Finkbeiner et al. 2002; Casassus et al. 2006, 2008; Dickinson et al. 2009, 2010; Scaife et al. 2009). The best examples are diffuse clouds within the Perseus (Watson et al. 2005) and ρ Ophiuchi (Casassus et al. 2008) regions, which have high-precision spectra showing the characteristic 'bump' (in flux density) at a frequency of $\approx 30 \,\mathrm{GHz}$ and can be fitted by plausible physical models for the spinning dust grains (Tibbs et al. 2011; Planck Collaboration XX 2011b). A survey of bright Galactic clouds in the Planck data (Planck Collaboration XV 2014c) has detected a number of potential candidates but follow-up observations at higher resolution are required to confirm them.

The origin of the diffuse AME found at high Galactic latitudes is still not clear (e.g. Hensley, Draine & Meisner 2016). Although spinning dust can readily account for the bulk of the AME (e.g. Planck Collaboration X 2016a), other emission mechanisms could be contributing (Planck Collaboration XXV 2016c), Magnetic dipole radiation from fluctuations in dust grain magnetization could be significant (Draine & Lazarian 1999; Draine & Hensley 2013; Hensley et al. 2016; Hoang & Lazarian 2016), although upper limits on AME polarization (Dickinson, Peel & Vidal 2011; López-Caraballo et al. 2011; Macellari et al. 2011; Rubiño-Martín et al. 2012; Génova-Santos et al. 2017) appear to indicate that this cannot account for the majority of the signal. Similarly, a harder (flatter spectrum) component of synchrotron radiation may also be responsible for AME, which was proposed by Bennett et al. (2003) at the time of the first WMAP data release. The harder spectrum naturally explains the correlation with dust, since both are related to the process of star formation. Furthermore, we already know that there are regions that have synchrotron spectral indices¹ that are at $\beta \approx -2.5$ or flatter, both supernova remnants (Onić 2013) and more diffuse regions such as the WMAP/Planck haze (Finkbeiner 2004; Planck Collaboration IX 2013b).

A harder synchrotron component may have been missed when applying component separation methods to microwave data. The majority of AME detections from fluctuations at high Galactic latitudes have been made using the 'template fitting' technique, i.e. fitting multiple templates for each foreground component to CMB data, accounting for CMB fluctuations and noise (Kogut et al. 1996; Banday et al. 2003). The synchrotron template is traditionally the 408 MHz all-sky map (Haslam et al. 1982), or another low-frequency template. However, data at these frequencies will naturally be sensitive to the softer (steeper spectrum) synchron emission, which has a temperature spectral index $(T \propto v^{\beta}) \beta \approx -3.0$ at frequencies \gtrsim 5 GHz (Davies, Watson & Gutierrez 1996; Davies et al. 2006; Kogut et al. 2007; Dunkley et al. 2009b; Gold et al. 2011). This leads to a significant AME signal at \sim 10–60 GHz that is correlated with FIR templates, which cannot be accounted for by the Rayleigh–Jeans tail of dust emission.

A hard synchrotron component of AME can be constrained (or ruled out) by using a higher radio frequency template of synchrotron emission. Peel et al. (2012) used the 2.3 GHz southern-sky survey of Jonas, Baart & Nicolson (1998) as a synchrotron template for the *WMAP* data and found that the dust-correlated AME component changed by only \approx 7 per cent, compared to using the 408 MHz template. This suggests that the bulk of the diffuse high-latitude synchrotron emission is indeed steep ($\beta \approx -3.0$) above 2.3 GHz, resulting in little change to the AME at 20–40 GHz.

The C-Band All-Sky Survey (C-BASS) is a survey of the entire sky at 5 GHz, in intensity and polarization, at a resolution of 45 arcmin (King et al. 2010; Jones et al. 2018). The frequency chosen is ideal for CMB component separation studies, being much closer to observing frequencies used by CMB experiments, typically at 30 GHz and higher. The northern survey (King et al. 2014) observations are complete and will be described in forthcoming papers. First results from the bright Galactic plane emission have been presented by Irfan et al. (2015).

In this paper, we present a preliminary C-BASS intensity map at 5 GHz of the North Celestial Pole (NCP) region, primarily based on the joint-fitting of spatial templates at a given frequency (e.g. Davies et al. 2006). The NCP area is known to have significant AME and FIR emission from the Polaris flare region, sometimes known as 'the duck' (Davies et al. 2006), having been studied in the first identification of AME (Leitch et al. 1997). The AME is relatively bright, while the synchrotron and free–free components appear to be weak, and their morphology is distinct from the AME/FIR emission. Furthermore, the older surveys of Haslam et al. (1982) at 408 MHz and Reich & Reich (1986) at 1.4 GHz are clearly affected by varying zero-levels, which appear as stripes in these maps. Also, due to the C-BASS scan strategy, the NCP region is observed very deeply by the C-BASS northern telescope, and has an almost negligible level of instrumental noise.

Section 2 describes the C-BASS observations and data analysis. Maps are presented in Section 3. The template-fitting results and foreground spectral energy distributions (SEDs) are presented in Section 4. A discussion of the results for each component is given in Section 5. Conclusions are summarized in Section 6.

2 OBSERVATIONS AND DATA ANALYSIS

The C-BASS project is surveying the entire sky, in intensity and polarization, at a nominal frequency of 5 GHz and an angular resolution of \approx 45 arcmin (Jones et al. 2018). It uses two telescopes to obtain full-sky coverage; the northern telescope is a 6.1-m Gregorian antenna situated at the Owens Valley Radio Observatory, California, and the southern telescope is a 7.6-m Cassegrain antenna situated at Klerefontein, the MeerKAT/SKA South Africa support

¹We use brightness temperature spectral indices, given by the definition $T_b \propto v^{\beta}$, which are related to flux density spectral indices by $\alpha = \beta + 2$.

base. The northern instrument was commissioned in 2009–2012 (Muchovej et al., in preparation) and observed routinely until 2015 April, after which the receiver was decommissioned. The southern instrument is currently carrying out the southern part of the survey.

2.1 Observations

The C-BASS scan strategy consists of 360° scans in azimuth at a constant elevation, at a speed of $\approx 4^{\circ}$ azimuth per second. The majority of the northern survey data were taken at elevations of $37^{\circ}.2$ (therefore passing through the NCP) and $47^{\circ}.2$, with additional scans at $67^{\circ}.2$ and $77^{\circ}.2$ to improve coverage at intermediate declinations. For the NCP region, only data at the two lower elevations are relevant, since higher elevations do not pass through the NCP region. However, the higher elevation data are useful in reducing the effects of drifts in the data due to 1/f noise (Taylor et al., in preparation).

The C-BASS receiver is a continuous-comparison radiometer (King et al. 2014), which measures the difference between sky brightness temperature and a stabilized resistive load. This architecture reduces receiver 1/f noise, which would otherwise be indistinguishable from variations on the sky. The receiver also implements a correlation polarimeter. However, no polarization data are used in this analysis. In this paper, we use data taken from the C-BASS North survey, covering the period 2012 November–2015 March.

2.2 Data analysis

The data have been processed using the latest version of the standard C-BASS data reduction pipeline. A detailed description of the pipeline will be given in forthcoming papers. In brief, the reduction pipeline identifies and flags out events of radio frequency interference, performs amplitude and polarization calibration, and applies atmospheric opacity corrections. It also removes contamination due to microphonics caused by the cryocooler cycle, which introduce oscillations in the output signal at a frequency of 1.2 Hz and harmonics thereof. Residual 1.2 Hz contamination is estimated to be at a level comparable to the thermal noise. The pipeline also removes large-scale ground spillover. Ground templates are made for each day of observations by subtracting the current best sky model from the time-ordered data, masking the strongest regions of Galactic emission, and binning in azimuth. This azimuth template is then subtracted from the time-ordered data before mapping. As well as removing the majority of the ground emission, this process inevitably removes a small fraction of the right-ascension-averaged sky signal. This is a significant effect on large angular scales but is not expected to be a major issue in the small region at the NCP analysed here. This effect will be mitigated in future analyses by including data from the southern survey, which have very different ground contamination at a given sky position. The current analysis also uses data taken only when the Sun is below the horizon, and all data within 5° of the Moon are also flagged.

The northern receiver includes a noise diode which, when fired, injects a signal of constant temperature. The pipeline calibrates the intensity signal on to the noise diode scale, and the noise diode is subsequently calibrated to the astronomical sources Cas A and Tau A. The calibrator flux densities are calculated from the spectral forms given in Weiland et al. (2011). The noise diode temperature is stable to within 1 per cent over time periods of several months and atmospheric opacity corrections are typically < 1 per cent, resulting in relative calibration uncertainties of ≈ 1 per cent (Irfan 2014).

The northern receiver has a nominal bandpass of 4.5–5.5 GHz but in-band filters to remove terrestrial RFI reduce the effective bandwidth to 0.499 GHz with a central frequency of 4.783 GHz. The effective observing frequency depends on the calibrator source and the source spectrum being observed but we do not attempt to colour correct the data considered in this paper as these corrections are of order 1 per cent. Since our main calibrator is Tau A ($\beta = -2.3$), and the bulk of the emission seen by C-BASS is steeper-spectrum synchrotron ($\beta \approx -3$), the effective frequency will be slightly lower than this by $\approx 0.05-0.1$ GHz. We therefore assume an effective frequency of 4.7 GHz throughout this paper.

The initial absolute calibration of the C-BASS maps is computed in terms of antenna temperature, which corresponds to the sky convolved with the full C-BASS beam. Since there is a significant (≈25 per cent; Holler et al. 2013) amount of power outside of the main beam, the conversion to brightness temperature depends on the angular scale of interest. In previous work, a common way around this issue has been to correct the scale to the 'main beam' (point source) or 'full beam' (extended source) scale to account for power lost to the far sidelobes (e.g. Reich 1982; Jonas et al. 1998). For a previous C-BASS paper (Irfan et al. 2015), we used a single factor of 1.124 to convert to an effective full-beam temperature scale for angular scales of a few degrees.

For the analysis in this paper, we use the theoretical beam calculated using the GRASP physical optics package (Holler et al. 2013) to deconvolve the sidelobe response while smoothing to an effective Gaussian resolution of 1° full width at half-maximum (FWHM). This produces maps with the correct resolution and smoothing function and it also results in a brightness temperature scale that is not dependent on angular scale. We find that the flux densities of bright sources agree with previous measurements to within $\approx\!\!5$ per cent. Since in this analysis we do not take into account the effects of a finite bandpass (colour corrections), we will adopt 5 per cent as our absolute calibration uncertainty. With future C-BASS data releases, and taking into account colour corrections, we expect to be able to reach $\approx\!\!1$ per cent accuracy.

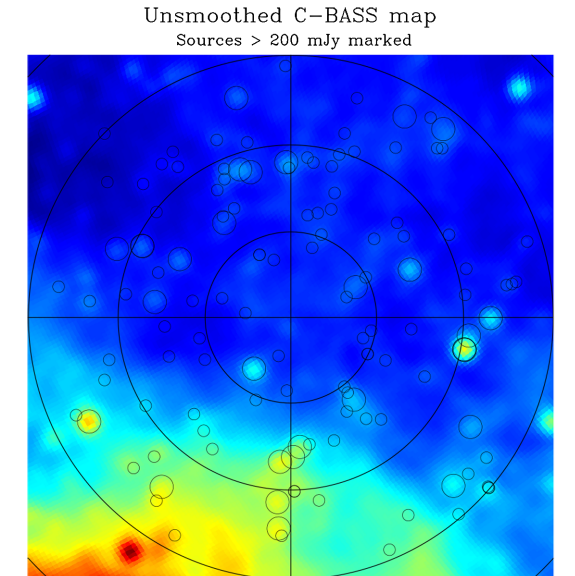
The C-BASS maps are made by the DEStriping CARTographer, DESCART (Sutton et al. 2010). DESCART performs a maximum likelihood fit to the contribution of 1/f noise in our timestreams with a series of offsets to the signal baseline, in this case 5 s long. Different scans are given the same optimal σ^{-2} weighting as is used in full maximum likelihood mapping, and are treated as independent. Variances were estimated from the power spectrum of the data. White-noise correlation between the channels is neglected for this work. The C-BASS data are made into healpix (Górski et al. 2005)² maps at $N_{\rm side} = 256$, corresponding to pixels ≈ 13.4 arcmin on-a-side.

3 MAPS

3.1 C-BASS NCP map

The unsmoothed C-BASS 5 GHz map of the NCP region is shown in the top panel of Fig. 1. The image is a gnomonic projection of the healpix $N_{\rm side}=256$ map, in units of mK (Rayleigh–Jeans), and with an angular resolution of 45 arcmin FWHM. An approximate zero level has been removed by subtracting the global minimum in the map to ensure positivity; the results are insensitive to this global offset. The map contains hundreds of radio sources

²http://healpix.sourceforge.net.



C-BASS integration

38.3 mK

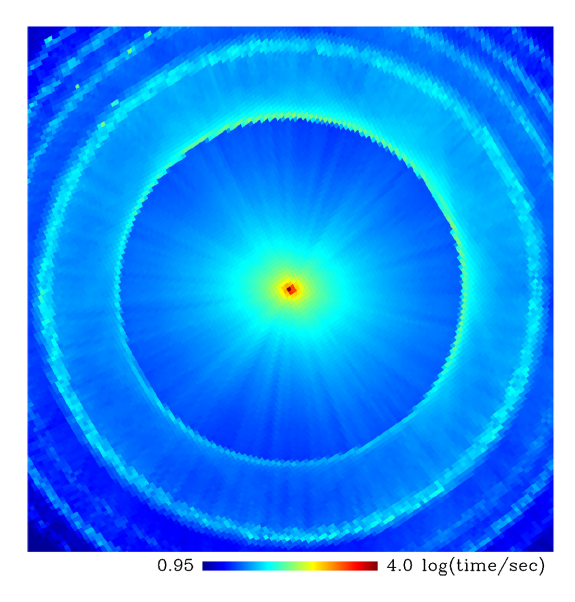


Figure 1. *Top*: Unsmoothed C-BASS 5 GHz $N_{\rm side}=256$ map of the NCP region at an angular resolution of 45 arcmin FWHM. The map covers a $30^\circ \times 30^\circ$ region centred at the NCP ($\delta=+90^\circ$) with RA = 0° at the bottom of the map (RA = 180° at the top) and increasing clockwise. The circular graticule lines mark 5° intervals in declination. The colour scale is linear between the minimum/maximum values shown. Radio sources with flux densities >200 mJy and $\delta>+75^\circ$ from the Mingaliev et al. (2007) catalogue are indicated by circles, with larger circles for flux densities >600 mJy. *Bottom*: Map of integration time (s) per $N_{\rm side}=256$ pixel on a logarithmic scale. The NCP region has the deepest integration in the C-BASS data. The circular rings correspond to the higher declination limits where the telescope is turning around, resulting in higher hit counts.

superposed on to diffuse Galactic emission; sources brighter than 200 mJy at 4.85 GHz and at $\delta > +75^{\circ}$ are marked with small circles. The majority of the radio sources are extragalactic and will be discussed further in Section 3.2. The diffuse emission is expected to be primarily synchrotron radiation, with a contribution of free–free

emission from our Galaxy. The Galactic plane is located towards the bottom of the map where the brightest emission is located.

The integration time for each $N_{\rm side} = 256 \ (\approx 13.4 \ {\rm arcmin\ on-a-}$ side) pixel is shown in the lower panel of Fig. 1. The integration time in the NCP region is very high everywhere due to the constant elevation scans that repeatedly cross the NCP region. The median integration at $\delta > +80^{\circ}$ is 50 s per $N_{\text{side}} = 256$ pixel, and much higher in the centre of the map. For the analyses at $N_{\rm side} = 64$ $(\approx 55.0 \text{ arcmin pixels})$, the integration time is effectively 16 times this value, i.e. ≈ 800 s. For the typical C-BASS rms noise level of \approx 2.0 mK s^{1/2} in intensity, this corresponds to a map rms noise level of ≈0.07 mK or better. Compared to the Galactic signal of several mK, the instrumental noise is therefore effectively negligible in this region. The typical rms confusion noise from fluctuations in the background of radio sources at this angular resolution is $\sim 0.6 \,\mathrm{mK}$ (Jones et al. 2018). The effects of a large number of weak sources can be seen in the colder regions of the C-BASS map (Fig. 1). Bright (\$\ge 200 \text{ mJy}) extragalactic sources will be removed from the C-BASS map before analysis (see Section 3.2).

The analysis was repeated on several versions of the C-BASS map, using a variety of data cuts and analysis procedures. Visual inspection of the maps showed the same structures at the same intensity level. Difference maps revealed low-level artefacts that were typically a few per cent or less of the signal of interest. The main contaminant was the Sun (via the far-out sidelobes of the C-BASS beam), which produced large-scale emission and scatter across the map, comparable to the Galactic emission in the NCP region. We therefore chose to use night-time only data, where this effect was eliminated. Nevertheless, we found that the results were consistent within the quoted uncertainties.

3.2 Extragalactic radio sources in the NCP region

It is clear that there is a significant contribution from extragalactic sources in the C-BASS data. The large beam of C-BASS means that the point-source flux density sensitivity is modest and we are limited by source confusion. The brightest sources are easily discernible in the C-BASS map (Fig. 1). Fortunately, a number of high angular resolution radio surveys have been made of the region, and they can be used to either mask or remove the brightest sources.

Kühr et al. (1981a) S5 survey mapped the NCP region ($\delta > +70^{\circ}$) with the Effelsberg 100-m telescope, with 476 detected sources, and is complete down to 250 mJy. Unfortunately, an electronic version of this catalogue is not currently available. The Kühr et al. (1981b) 5 GHz catalogue of bright (>1 Jy) sources contains only seven sources at $\delta > +80^{\circ}$. The Green Bank 6-cm radio source catalogue (Gregory et al. 1996) is a blind survey complete to \approx 18 mJy but is limited to $\delta < +75^{\circ}$ and therefore is not useful here. The NRAO VLA All-Sky Survey (NVSS; Condon et al. 1998) at 1.4 GHz is the highest frequency unbiased radio survey that covers $\delta > +88^{\circ}$; it contains hundreds of radio sources but the majority are \sim 3-100 mJy and cannot be accurately extrapolated to 5 GHz. Healey et al. (2009) surveyed the region at 4.85 GHz but pre-selected sources that were flat spectrum. They measured three sources in this relatively unobserved region ($\delta > +88^{\circ}$) at 4.85 GHz with flux densities of 67, 58, and 142 mJy, respectively. Ricci et al. (2013) made 5-30 GHz measurements of bright sources detected in the K-band Medicina pilot survey (Righini et al. 2012).

The only other radio survey of the NCP region ($\delta > +75^{\circ}$) at frequencies above 1.4 GHz is the RATAN-600 multifrequency survey of Mingaliev et al. (2007), which includes measurements at 4.8 GHz. They observed 504 sources from the 1.4 GHz NVSS that

were located $+75^{\circ} < \delta < +88^{\circ}$ and had a flux density $S_{1.4\,\mathrm{GHz}} > 0.2\,\mathrm{Jy}$. We therefore use the 4.8 GHz catalogue of Mingaliev et al. (2007) for identifying and masking sources in the NCP region.

The locations of radio sources above 200 mJy from Mingaliev et al. (2007) are overplotted in Fig. 1. The brightest sources (>600 mJy) at δ > +80° are listed in Table 1. Virtually all of these sources at δ > +75° lie on peaks in the C-BASS map. This is reassuring and indicates that we understand well the bright source population at 5 GHz. However, it should be noted that a number of these sources exhibit variability in their flux density (e.g. Liu et al. 2014). The brightest source in our field (δ > +80°) away is the double-lobed radio galaxy 3C 61.1, which has a flux density of \approx 2 Jy at 4.7 GHz (Hargrave & McEllin 1975).³

Fig. 2 shows the map of point sources, convolved with a 1° FWHM Gaussian beam. The fluctuations in brightness temperature are at the level of \approx 1–2 mK away from bright sources. The source 3C 61.1 has a peak brightness temperature of $\approx 9 \,\mathrm{mK}$ above the background. In the middle panel of Fig. 2, we show the C-BASS map after smoothing (and deconvolving) to the common 1° FWHM resolution. The right-hand panel shows the C-BASS map after subtracting the map of sources. Visual inspection shows that the subtraction has been successful, with most of the obvious sources no longer being visible. For the brightest few sources (3C 61.1, NGC 6251) the subtraction is not perfect. For example, NGC 6251 has been undersubtracted (possibly due to its large angular extent of over 1°). These could be removed by fitting for their flux densities separately. However, we choose to mask the four brightest sources with an aperture of 0.7 radius. We also mask out the NCP itself $(\delta = +90^{\circ})$ because there appears to be a relatively bright source in the C-BASS map, which is not in the majority of source catalogues. The source mask is shown in Fig. 2. Fainter sources can be either masked or subtracted, as a test of point-source contamination. Our results are not strongly sensitive to the effects of residual source contamination (see Section 4.2).

At the higher frequencies ($\gtrsim 20\,\mathrm{GHz}$) observed by WMAP and Planck, some of the weaker radio sources are much fainter than at lower frequencies because many galaxies have spectral indices $\alpha < 0$ (flux density $S \propto \nu^{\alpha}$). The main population of radio sources at frequencies $\gtrsim 20\,\mathrm{GHz}$, particularly at high flux densities, are galaxies that harbour active galactic nuclei (AGN), which can produce flat-spectrum radiation up to tens of gigahertz or even higher. In the NCP region ($\delta > +75^{\circ}$), the Planck compact source catalogue, PCCS2 (Planck Collaboration XXVI 2016d), contains 28 sources above 0.5 Jy while only three sources are above 1 Jy. Of these, only one source (NGC 6251) is in the $\delta > +80^{\circ}$ region, with a 28.4 GHz flux density of 1.3 \pm 0.1 Jy. Pixels affected by this source will be masked out.

3.3 Multifrequency maps of the NCP region at 1° resolution

We now compare the C-BASS data with multifrequency radio, microwave, and FIR data. The data sets are summarized in Table 2. The absolute calibration uncertainties are those assumed later in

the analysis. Data from *WMAP* 9 yr (Bennett et al. 2013) and *Planck* 2018 results (PR3) (Planck Collaboration I 2018a) are the primary data being analysed. We assume a conservative minimum 3 per cent (5 per cent) uncertainty for *WMAP/Planck* LFI (HFI) data primarily due to not applying colour corrections. The uncertainty encompasses any additional errors such as those due to beam asymmetries and other potential low (<1 per cent) level errors.,

We include low-frequency radio data from the Haslam et al. (1982) 408 MHz and 1.42 GHz Reich & Reich (1986) surveys. Both maps have been filtered to remove the brightest point sources and stripes due to scanning artefacts. At 408 MHz, we choose to use the improved destriped and desourced version of Remazeilles et al. (2015) although the results are consistent between the two. For the 1.42 GHz data we use the full-sky version, which has been destriped and desourced (Reich 1982; Reich & Reich 1986; Reich, Testori & Reich 2001). The 1.42 GHz map has been multiplied by a factor of 1.55 to place it on the 'full-beam' scale, appropriate for diffuse foregrounds (W. Reich, priv. comm.). We assume a nominal 10 per cent calibration uncertainty for both maps.

As tracers of free–free emission, we use the full-sky H α maps of Dickinson et al. (2003) (D03) and Finkbeiner (2003) (F03), both of which are based on Wisconsin H-Alpha Mapper (WHAM; Haffner et al. 2003) data. Both versions contain nominal corrections for dust extinction, which are modest (\lesssim 0.2 mag) at intermediate and high Galactic latitudes, and therefore possible errors in the corrections are not critical

As tracers of dust (thermal dust and AME), we use several different template maps, listed in Table 2. Our primary dust template is the map of the thermal dust optical depth at 353 GHz, τ_{353} , based on *Planck* data (Planck Collaboration XI, XLVIII 2014a, 2016e), which is known to be a good tracer of the dust column density and is a good tracer of AME (Planck Collaboration XXV 2016c). As will be discussed in Section 5.3, this was found to be the best tracer of AME in the NCP region. We also use several other standard dust tracers including the IRIS reprocessed IRAS 100 μ m map by Miville-Deschênes & Lagache (2005), *Planck* HFI maps at 353, 545, and 857 GHz, the map of dust radiance \Re (Planck Collaboration XI, XLVIII 2014a, 2016e), and the FDS model 8 map at 94 GHz by Finkbeiner et al. (1999).

To facilitate the comparison, we smooth all the maps to a common 1° FWHM (Gaussian point spread function) angular resolution by smoothing the data with the appropriate Gaussian kernel (or the more accurate beam window functions in the case of *Planck* data) and re-sampled the maps to a common $N_{\rm side}=256$ HEALPIX grid. Fig. 3 displays 1° -smoothed maps of the NCP region. Strong Galactic emission is seen towards the bottom of the maps in the direction of the Galactic plane. Point sources are evident, especially at the lower frequencies. AME is directly visible at frequencies $\sim\!20\!-\!40$ GHz near the centre of the map, with morphology that resembles thermal dust emission at higher frequencies (e.g. 545 GHz), FIR (e.g. $100~\mu m$), and τ_{353} .

The low-frequency radio maps at 0.408 and 1.42 GHz show clear residual scanning artefacts. These are visible as striations emanating radially outwards from the NCP. This is particularly noticeable in the 0.408 GHz map. The C-BASS 4.7 GHz map on the other hand shows no obvious visible artefacts. The 1.42 GHz map also appears to contain diffuse structure near the NCP that is not visible in either of the 0.408 or 4.7 GHz maps, or in H I 21 cm maps (Winkel et al. 2016), and is likely to be an artefact. Nevertheless, none of the low-frequency maps, including C-BASS 4.7 GHz, show emission that resembles the AME seen at 20–40 GHz. Given the higher frequency of the C-BASS data, and improved map fidelity, it should be a much

 $^{^3}$ Mingaliev et al. (2007) catalogue reports a flux density for 3C 61.1 of 970 ± 80 mJy at 4.8 GHz, which is inconsistent with various measurements of ≈ 1.9 Jy at 5 GHz (the source is not thought to be significantly variable). Since they report three individual sources (they do not give the flux densities for these due to confusion of multiple sources hence the 'X's in the catalogue entry) it may be that this is a typographical error in which they have reported one of the contributing sources. Other sources appear to be unaffected.

Table 1. List of bright (>600 mJy) sources in the NCP region (δ > +80°), ordered in decreasing flux density. Flux densities at 4.8 GHz are taken from Mingaliev et al. (2007), except for 3C 61.1* (see text and footnote³), which is taken from Hargrave & McEllin (1975). The uncertainties are dominated by 3 per cent calibration errors.

Source	Flux density (mJy)	(RA, Dec.) [J2000] (deg)	(<i>l</i> , <i>b</i>) (deg)	Alternate name	
115312+805829	2130	(178.30, +80.97)	(125.72, +35.84)	S5 0014+81	
0222XX+86XXXX*	1900	(35.70, +86.31)	(124.49, +23.72)	3C 61.1	
234403+822640	1433	(356.02, +82.44)	(120.61, +19.88)	S5 1150+81	
104423+805439	1404	(161.10, +80.91)	(128.74, +34.74)	S5 1039+81	
001708+813508	1190	(4.29, +81.59)	(121.61, +18.80)	S5 0014+81	
075058+824158	1061	(117.74, +82.70)	(130.99, +28.77)	S5 0740+82	
074305+802544	804	(115.77, +80.43)	(133.60, +28.86)	3C 184.1	
062602+820225	751	(96.51, +82.04)	(131.74, +25.97)	S5 0615+82	
163226+823220	749	(248.11, +82.54)	(115.77, +31.20)	NGC 6251	
074246+802741	698	(115.70, +80.46)	(133.56, +28.85)	3C 184.1	
093923+831526	672	(144.85, +83.26)	(128.81, +31.52)	3C 220.3	
161940+854921	670	(244.92, +85.82)	(119.14, +29.65)	S5 1631+85	
213008+835730	656	(322.54, +83.96)	(117.88, +23.18)	3C 435.1	
235622+815252	626	(359.10, +81.88)	(120.89, +19.23)	S5 2353+81	
105811+811432	601	(164.55, +81.24)	(127.97, +34.75)	S5 1053+81	

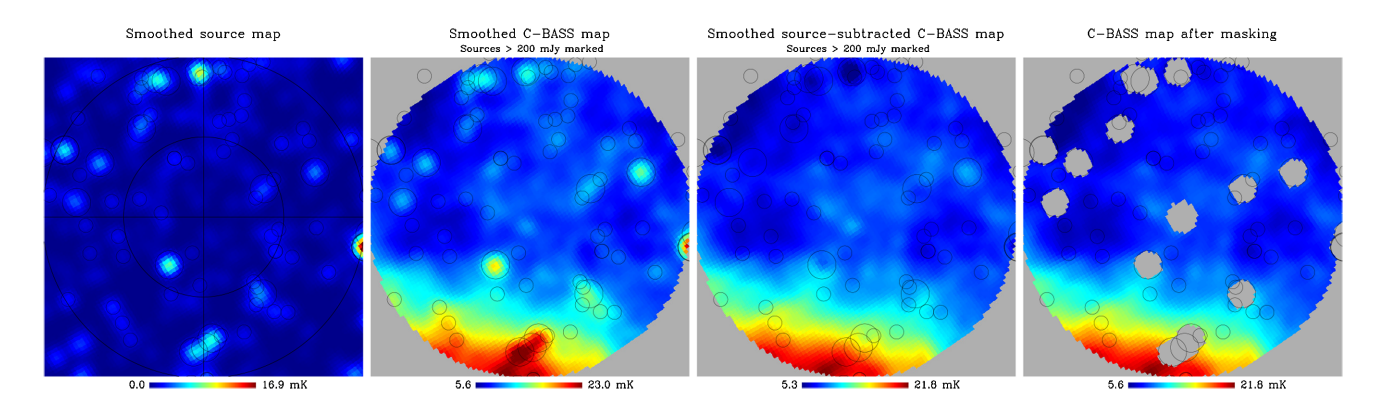


Figure 2. From *left* to *right*: (i) Map of bright (>200 mJy) sources from the Mingaliev et al. (2007) catalogue after convolving with a 1° FWHM Gaussian beam. (ii) C-BASS map, smoothed to 1° FWHM resolution. (iii) C-BASS map after subtracting bright extragalactic sources. (iv) C-BASS map with masked regions shown as grey ($\delta < +80^{\circ}$, the brightest sources, and for $\delta > +89^{\circ}$; see text). The coordinate system is the same as in Fig. 1 but covering $\delta > +80^{\circ}$. Bright sources above 200 and 600 mJy are marked as small and large circles, respectively. The colour scale is linear between the minimum/maximum values shown.

more reliable foreground template for synchrotron emission. This will be quantified in detail in Section 4.

The H α maps contain low-level fluctuations at the level of \approx 1 R. However, the structure in the two versions of the map (D03 and F03) differs in detail, particularly in the central region where the AME is most prominent. Although the original data were the same, there were significant differences in the processing of the data. In particular, removal of stellar residuals in the H α maps is difficult and can result in artefacts at the level of \approx 1 R. We will compare the results of both maps to see how different they are and which one is most consistent with theoretical expectations.

To understand how the structure in these maps correlates, we begin by plotting the pixel intensities of each map against other maps, i.e. T–T plots (Turtle et al. 1962). The data are first smoothed to a common 1° FWHM resolution and downgraded to $N_{\rm side}=64$ (≈ 55 arcmin pixels) to reduce correlations and make each pixel quasi-independent. For clarity and to reduce the correlations from the nearby Galactic plane, we only plot pixels at $\delta > +83^\circ$. This helps isolate the AME clouds away from the plane and reduces the number of plotted symbols in the figures.

Fig. 4 shows T-T plots for several combinations of radio data, microwave data (specifically the 22.8 GHz WMAP map), Planck 545 GHz map, *Planck* thermal dust optical depth map (τ_{353}) , and H α (D03 and F03). Pixels that are masked for the brightest (>600 mJy) sources are marked as red stars while pixels containing known sources above 200 mJy at 4.8 GHz are marked as filled blue circles. It is reassuring to see that there is good correlation of the radio maps at 0.408, 1.42, and 4.7 GHz. However, there is significant scatter (Pearson correlation coefficient, $r \approx 0.7$) which would not be expected given the high-signal-to-noise ratio of these maps. Part of this may be due to variations in the synchrotron spectral index across the map and free-free emission, or to differences in source subtraction in the maps. However, inspection of the maps (Fig. 3) clearly reveals artefacts in the maps that are likely responsible for the majority of the scatter. The brightest sources (red stars in Fig. 4) can be seen to have some effect in some of the radio maps, pushing the intensities to larger values, but in general they are not a major issue; the C-BASS data have been source-subtracted and those pixels containing sources above 600 mJy are masked in the analysis.

2850 C. Dickinson et al.

Table 2. Summary of multifrequency data. The *top* part of the table represent the various foreground templates that will be fitted to the microwave/sub-mm (*WMAP/Planck*) data, which are listed in the *bottom* part of the table. The listed absolute calibration errors are those assumed for deriving spectral indices (see text).

Telescope/Survey	Freq. (GHz)	Ang. res. (arcmin)	Abs. Cal. Error (per cen	Reference t)	Notes
Haslam	0.408	51	10	Haslam et al. (1982) and Remazeilles et al. (2015)	Synchrotron template
Reich	1.42	36	10	Reich & Reich (1986)	Synchrotron template
C-BASS	4.7	45	5	This work	Synchrotron template
F03 H α	_	6/60	10	Finkbeiner (2003)	Free-free template
D03 H α	_	60	10	Dickinson et al. (2003)	Free-free template
Planck PR3 HFI 353 GHz	353	4.7	5	Planck Collaboration I (2018a)	Dust template (vR3.00)
Planck PR3 HFI 545 GHz	545	4.73	5	Planck Collaboration I (2018a)	Dust template (vR3.00)
Planck PR3 HFI 857 GHz	857	4.51	5	Planck Collaboration I (2018a)	Dust template (vR3.00)
Planck 353 GHz optical depth	353	5.0	5	Planck Collaboration XLVIII (2016e)	Dust template (vR2.00)
Planck dust radiance R	_	5.0	_	Planck Collaboration XI, XLVIII (2014a, 2016e)	Dust template
IRAS (IRIS) 100 μm	2997	4.3	13.5	Miville-Deschênes & Lagache (2005)	Dust template
FDS94 model 8	94	6.1	_	Finkbeiner, Davis & Schlegel (1999)	Dust template
<i>WMAP</i> 9-yr <i>K</i> band	22.8	51.3	3	Bennett et al. (2013)	1°-smoothed product
Planck PR3 LFI 30 GHz	28.4	33.16	3	Planck Collaboration I (2018a)	vR3.00
<i>WMAP</i> 9-yr <i>Ka</i> band	33.0	39.1	3	Bennett et al. (2013)	1°-smoothed product
<i>WMAP</i> 9-yr <i>Q</i> band	40.7	30.8	3	Bennett et al. (2013)	1°-smoothed product
Planck PR3 LFI 44 GHz	44.1	28.09	3	Planck Collaboration I (2018a)	vR3.00
<i>WMAP</i> 9-yr <i>V</i> band	60.7	30.8	3	Bennett et al. (2013)	1°-smoothed product
Planck PR3 LFI 70 GHz	70.4	13.08	3	Planck Collaboration I (2018a)	vR3.00
<i>WMAP</i> 9-yr <i>W</i> band	93.5	30.8	3	Bennett et al. (2013)	1°-smoothed product
Planck PR3 HFI 100 GHz	100	9.59	5	Planck Collaboration I (2018a)	vR3.00
Planck PR3 HFI 143 GHz	143	7.18	5	Planck Collaboration I (2018a)	vR3.00
Planck PR3 HFI 217 GHz	217	4.87	5	Planck Collaboration I (2018a)	vR3.00
Planck PR3 HFI 353 GHz	353	4.7	5	Planck Collaboration I (2018a)	vR3.00
Planck PR3 HFI 545 GHz	545	4.73	5	Planck Collaboration I (2018a)	vR3.00
Planck PR3 HFI 857 GHz	857	4.51	5	Planck Collaboration I (2018a)	vR3.00

The best-fitting straight line, y=mx+c, is plotted for each combination of data sets, taking into account uncertainties in both coordinates using the MPFITEXY⁴ routine (Markwardt 2009; Williams, Bureau & Cappellari 2010). Only unmasked pixels are included in the fit. The slope, m, of each T–T plot between frequencies v_1 and v_2 , is related to the spectral index by $\beta = \ln(m)/\ln(v_1/v_2)$. The spectral index⁵ between 0.408 and 1.42 GHz is $\beta = -2.95 \pm 0.65$, which is indicative of steep synchrotron radiation. Note that we have rescaled the uncertainties to take into account the scatter in the data by scaling the uncertainties until $\chi_r^2 = \chi^2/\nu = 1$, where ν is the number of degrees of freedom. For the cases where there is significant scatter, this increases the fitted uncertainties by a factor of several.

The spectral index between 0.408 and 4.7 GHz is $\beta = -2.79 \pm 0.17$ and between 1.42 and 4.7 GHz it is $\beta = -2.57 \pm 0.77$. These are consistent with typical values at these frequencies of $\beta \approx -2.8$ with variations of $\Delta \beta \approx 0.2$ (Reich & Reich 1988; Davies et al. 1996; Platania et al. 1998). There is a hint of a slight flattening at higher frequencies, but at less than 1σ confidence level. If this were the case, we would expect to see this reflected in the cross-correlation (CC) analysis (Section 4) when using the C-BASS data as a synchrotron template, which will be discussed further in Section 5.1. Note that the T-T spectral index between

22.8 and 44.1 GHz is $\beta=-3.01\pm0.06$, which is similar to that of synchrotron radiation. However, as we show in Sections 4 and 5 below, it is actually primarily due to AME. Indeed, the T–T spectral index from 4.7 to 22.8 GHz has a flatter value of -2.44 ± 0.74 which suggests a new component is contributing, while the large scatter (and hence larger uncertainty) shows that the two maps are not tightly correlated, with a Pearson correlation coefficient of $r=0.48\pm0.06$.

The lack of perfect correlation between the two versions of the H α map, D03 and F03 ($r=0.81\pm0.03$), given that they are constructed essentially from the same data, confirms the significant differences between them already noted. The correlation between D03 and the microwave maps at 20–40 GHz is much stronger ($r=0.70\pm0.04$ at 22.8 GHz) than for the F03 map ($r=0.24\pm0.08$). Given that the maps were created independently of the microwave data at a completely different wavelength (in this case, at optical wavelengths), this suggests that the D03 map may be more reliable, at least for this region. We will therefore use the D03 H α map for the main results, but will also consider F03 to test how sensitive the results are to changes in the free–free template (see Section 5.2).

The most important result here is that the dust-correlated AME emission clearly visible at 22.8 GHz (and frequencies in the range \approx 20–40 GHz) is not visible at 4.7 GHz. The T–T plot (Fig. 4) shows that there is some correlation between 4.7 and 22.8 GHz ($r=0.48\pm0.06$), but 4.7 GHz is much less correlated with FIR dust emission than the microwave frequencies are. For example, the correlation coefficient between 22.8 GHz and 100 μ m is $r=0.88\pm0.02$, and 22.8 GHz and τ_{353} gives an even tighter correlation

⁴http://purl.org/mike/mpfitexy.

⁵Unless otherwise stated, uncertainties in spectral indices include an absolute calibration error term, given in Table 2, which is added in quadrature with the intrinsic noise uncertainty.

⁶We use the /REDUCE option in the MPFITEXY code.

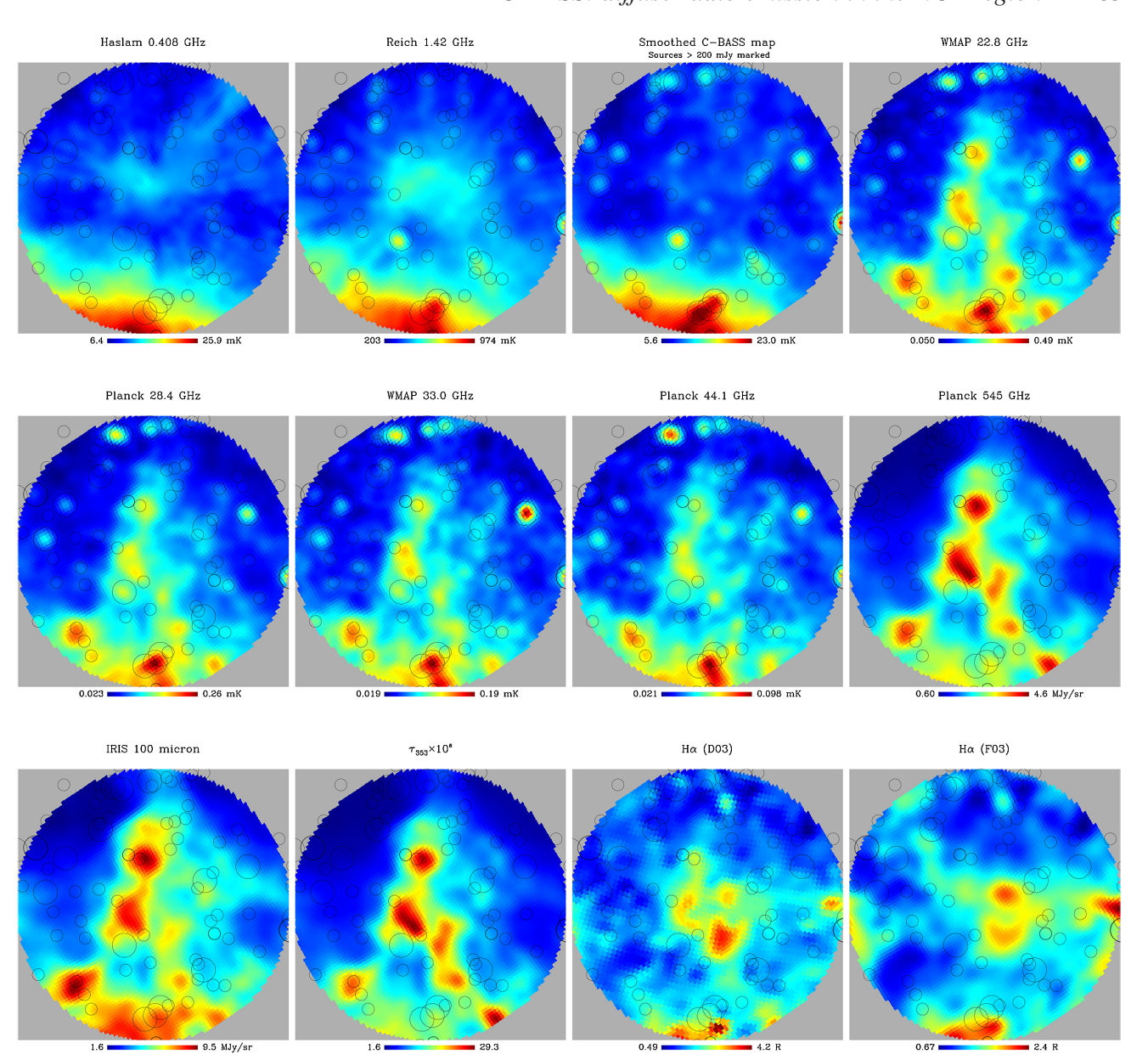


Figure 3. Multifrequency maps of the NCP region at a common resolution of 1° (see Table 2 for details). The panels are arranged in increasing frequency order: 0.4, 1.42, 4.7, 22.8, 28.4, 33.0, 41.0, 545, 3000 GHz (100 μm). The last three panels are τ_{353} , followed by two versions of the Hα map (D03 and F03). The colour scales are all on a linear stretch between the minimum/maximum values shown. The coordinate system is the same as in Fig. 1 but covering $\delta > +80^\circ$. Radio sources are indicated by circles as in previous figures. The dust-correlated AME structure (e.g. at 545 GHz, 100 μm, τ_{353}) is clearly visible at 22.8 and 28.4 GHz but not at 4.7 GHz. Striations and other artefacts are also visible in the 0.408/1.42 GHz maps that are not seen in the C-BASS data.

of $r=0.93\pm0.01$, while the correlation between 4.7 GHz and τ_{353} is only $r=0.23\pm0.08$. As noted previously (e.g. Tibbs et al. 2013; Planck Collaboration XXV 2016c) the AME appears to correlate better with τ_{353} (which is approximately proportional to the line-of-sight column density) than with the FIR such as $100\,\mu\text{m}$.

In summary, the AME visible at 20–40 GHz does not appear to be related to the emission at 4.7 GHz and below, i.e. synchrotron or free–free radiation. This will be quantified further in Section 4. Nevertheless, even without further analysis, these morphological comparisons suggest that unaccounted synchrotron and free–free emission cannot be responsible for the majority of the AME in the NCP region.

4 TEMPLATE FITTING

4.1 Template fitting method

To separate the contributions of the diffuse foreground components, we will use the different spatial morphologies, as traced by foreground template maps. Table 2 summarizes the data sets that are used and the ancillary data on which the foreground templates are based. The template fitting method is well-known (see e.g. Ghosh et al. 2012 and references therein). Briefly, we assume the data vector \mathbf{d} at a given frequency is the sum of each template map vector \mathbf{t}_i multiplied by a template correlation coefficient, α_i . The data are then corrupted by noise \mathbf{n} , which can consist of various terms including instrumental noise, CMB fluctuations or point sources.

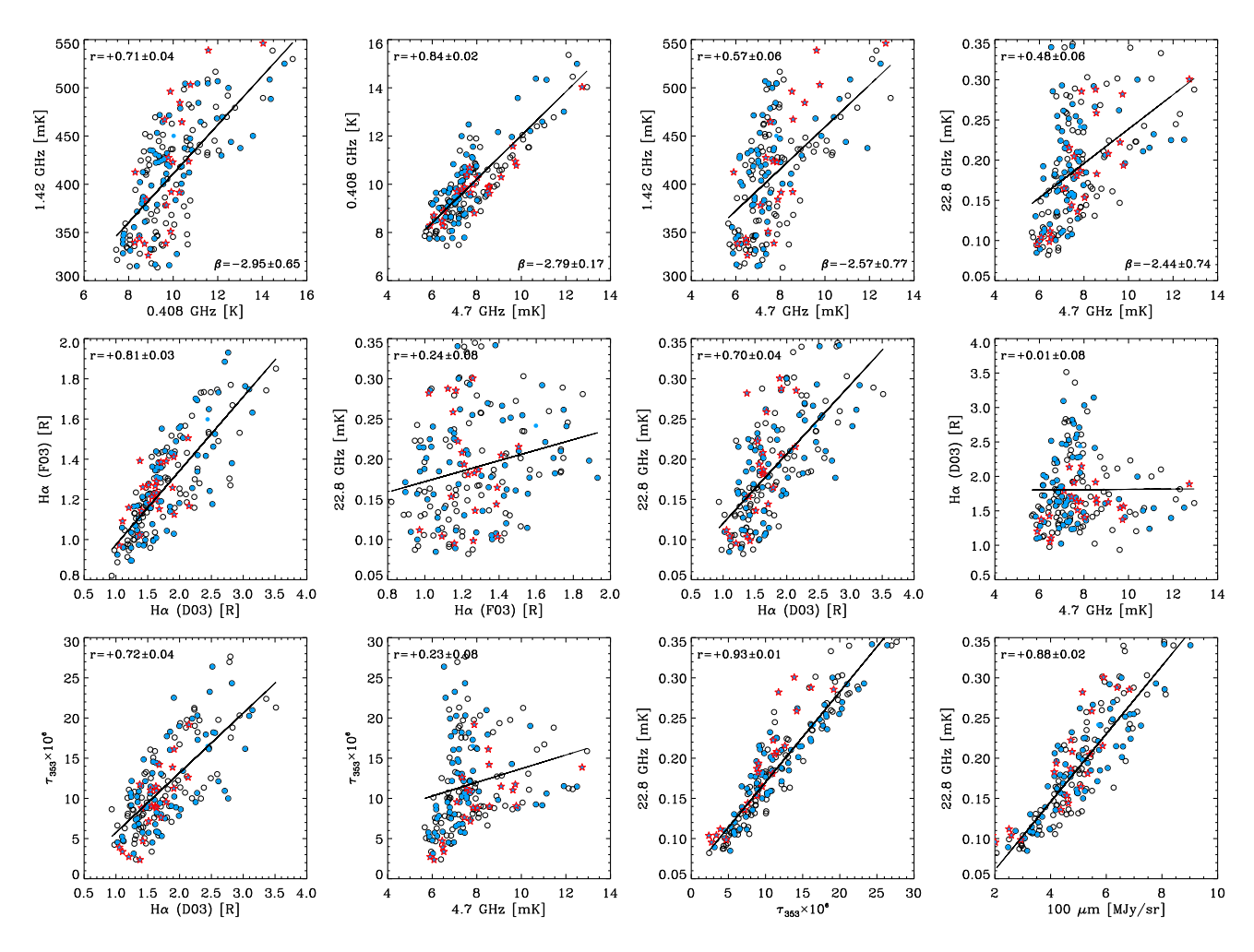


Figure 4. T–T plots of the NCP region ($\delta > +83^{\circ}$) for various combinations of maps. The *circles* are for pixels used for template fitting. *Blue filled circles* are pixels that contain a weak ($<600 \,\mathrm{mJy}$) extragalactic source from the Mingaliev et al. (2007) survey. *Red stars* are pixels that contain a bright ($>600 \,\mathrm{mJy}$) source and are excluded from the analysis and fits. The line is the best-fitting straight line to the data after masking (*unfilled* and *filled blue circles*). The corresponding spectral index β (where relevant) and Pearson correlation coefficient r are also shown in each plot.

For N templates (e.g. 3 foreground components and an offset term), the data vector reads

$$\mathbf{d} = \sum_{i}^{N} \alpha_{i} \mathbf{t}_{i} + \mathbf{n} . \tag{1}$$

The χ^2 for this model, allowing for correlations in noise between pixels is given by

$$\chi^2 = (\mathbf{d} - \alpha_i \mathbf{t}_i)^T \mathbf{C}^{-1} (\mathbf{d} - \alpha_i \mathbf{t}_i). \tag{2}$$

Here, the covariance matrix C contains all the sources of noise. In our analysis this can be instrumental noise (C_{noise}), CMB fluctuations (C_{CMB}), or extragalactic point sources (C_{PS}), i.e.

$$C = C_{\text{noise}} + C_{\text{CMB}} + C_{\text{PS}} . \tag{3}$$

For white, independent Gaussian noise, only the diagonal elements will be non-zero, and are equal to the variance σ^2 . We choose to degrade the maps to $N_{\rm side}=64$ (pixels ≈ 55 arcmin on-aside) for the CC analysis, which means that the instrumental noise is approximately diagonal. To take into account CMB fluctuations, we can add in the CMB covariance matrix, with prior knowledge of the CMB power spectrum C_ℓ . The CMB fluctuations are very close

to Gaussian, allowing the CMB covariance matrix to be calculated from the power spectrum alone. It is given by

$$C_{CMB} = \frac{1}{4\pi} \sum_{\ell} (2\ell + 1) C_{\ell} P_{\ell}(\cos \theta) W_{\ell},$$
 (4)

where $P_\ell(\cos\theta)$ is the Legendre polynomial order and the sum runs from $\ell=2$ (monopole and dipole are assumed to have been removed) to $\ell_{\rm max}=3N_{\rm side}-1$. W_ℓ is the window function, which accounts for the beam b_ℓ and pixel p_ℓ window functions. However, treating the CMB in this statistical way increases the uncertainties typically by a factor of ~ 5 or more. We therefore do not consider the non-subtracted maps further in this paper. For our final results, we instead directly remove the CMB by subtracting CMB maps produced using component separation algorithms and add in an additional term in the covariance matrix to account for the accuracy to which the CMB map is known (see Section 4.3).

By minimizing the χ^2 with respect to α_i , the coupling constant α_i can be estimated:

$$\alpha_i = \frac{\mathbf{t}_i \, \mathbf{C}^{-1} \, \mathbf{d}}{\mathbf{t}_i \, \mathbf{C}^{-1} \, \mathbf{t}_i} \tag{5}$$

and its Gaussian uncertainty is given by

$$\sigma^2(\alpha_i) = (\mathbf{t}_i \, \mathbf{C}^{-1} \, \mathbf{t}_i)^{-1} \,. \tag{6}$$

The contribution of component i to the observed sky is the map $\alpha_i T_i$, where T_i is in the natural units of the foreground template map so that this scaled quantity is in mK.

4.2 Contribution of point sources

As discussed in Section 3.2, there is a significant contribution from extragalactic point sources, both in the low-frequency radio maps and, to a lesser extent, the microwave maps. In this paper, we are interested in the diffuse Galactic emission and therefore this contribution must be quantified and mitigated. Our main strategy for point-source mitigation is to mask the brightest sources in the analysis. Smoothing the data to 1° resolution also reduces the impact of point-like sources.

We use the 4.8 GHz measurements of Mingaliev et al. (2007), who measured all sources brighter than 200 mJy in the 1.4 GHz NVSS catalogue (Condon et al. 1998). Pixels that have any part of their area within 0°.7 of a source with $S_{4.8} > 600$ mJy are masked. We varied this cut-off and found only a slight dependence when including pixels contaminated with sources above 600 mJy; below this cut-off, the results were consistent within the uncertainties. We also mask $\delta > +89^{\circ}$ because the measurements do not cover the very highest declinations ($\delta > +88^{\circ}$), where C-BASS appears to see at least one relatively bright (\sim 500 mJy) source very close to the NCP.

For the sources in the higher frequency maps (22.8 GHz and above), we can take the fainter sources into account statistically by including additional terms in the covariance matrix. Assuming sources are Poisson distributed, in the limit of a large number of sources N the map fluctuations tend to a Gaussian distribution, and the point source covariance matrix, C_{PS} becomes diagonal. The power spectrum of point sources is given from the source counts dN/dS by

$$C_{\ell}^{\text{PS}} = g(\nu)^2 \int_0^{S_{\text{max}}} S^2 \frac{\mathrm{d}N}{\mathrm{d}S} \mathrm{d}S ,$$
 (7)

where $g(v) = 2kv^2/c^2$ converts flux density *S* (in Jy) to brightness temperature units (K).

There are a number of measurements of source counts at frequencies near 20 GHz (e.g. de Zotti et al. 2010). We choose to use the simple power-law fit of AMI Consortium et al. (2011) to 15.7 GHz data from the 9C/10C surveys because they measure sources down to millijansky levels, well below our cut-off flux density limit of 0.6 Jy. They measure $dN/dS \approx 48S^{-2.13}\,\mathrm{Jy^{-1}}\,\mathrm{sr^{-1}}$ in the flux range from 2.2 mJy to 1 Jy. Integrating this function from 2.2 mJy to our nominal flux cut-off of 600 mJy (there were no sources brighter than this limit not being masked in the *Planck* point source catalogues) gives $\Delta T = 11.8\,\mu\mathrm{K}$ rms per $N_{\mathrm{side}} = 64$ pixel at 22.8 GHz. The contribution of faint sources is therefore small but not completely negligible and so we include this contribution in the noise covariance matrix in our analysis.

We choose not to scale the source counts from 15.7 GHz to the higher frequencies. The brighter sources are typically flat spectrum ($\alpha=0$) at frequencies relevant to AME (see e.g. de Zotti et al. 2010), and hence scaling of these is not necessary. The fainter sources are typically steep spectrum ($\alpha\approx-0.5$) and hence these give a smaller contribution to the source power at higher frequencies. This means that our uncertainties for this contribution will be slightly

overestimated at higher frequencies, but this has negligible impact on the results.

4.3 Template fitting of WMAP/Planck data

We apply the template fitting method to maps at $N_{\rm side}=64$, at which resolution the pixels are close to independent. The data vectors include pixels above a declination limit $\delta_{\rm lim}$, which we vary in the range $+75^{\circ} < \delta_{\rm lim} < +85^{\circ}$ to test the robustness of the results against the precise sky area. We quote the primary results for $\delta_{\rm lim}=+80^{\circ}$, which allows the two bright dust clouds in the region to be included as well as some of the brighter emission at lower Galactic latitudes. The results for different declinations were generally consistent within the uncertainties ($<2\sigma$), except for the synchrotron coefficient which varies by $\approx 4\sigma$ when considering just the inner portion of the map at $\delta > +83^{\circ}$; this is discussed in Section 5.1.

The best-fitting template coefficients are listed in Table 3. The coefficients represent the amount of emissivity at each WMAP/Planck frequency, relative to the template foreground component.⁷ We do not include absolute calibration uncertainties when quoting correlation coefficients or rms brightness temperatures. We focus on the lower channels of WMAP/Planck (22.8–44.1 GHz) where AME is strongest. We quote the results after direct removal of the CMB using the SMICA CMB map described in Planck Collaboration IV (2018b). Using alternative CMB maps from Planck (Commander, SEVEM, NILC) gave consistent results within the uncertainties. In this case we have assumed a conservative CMB residual 'noise' per pixel of 10 µK to account for the fact that the component separation is not perfect. This is informed by inspection of the four CMB maps described in Planck Collaboration IV (2016b, 2018b) where typical differences (away from bright sources) are of order 5 µK. This is comparable to the typical instrumental rms noise in the WMAP/Planck data at frequencies \sim 20–40 GHz at $N_{\rm side} = 64$.

We fit for a synchrotron component using either the Haslam et al. (1982) map (top part of Table 3) or the C-BASS 4.7 GHz map (bottom part). This allows us to test for a flatter-spectrum component of synchrotron radiation, which would be better traced by the higher frequency template from C-BASS.

The H\$\alpha\$-correlated (free–free) template is the D03 all-sky H\$\alpha\$ map (Dickinson et al. 2003), with a correction for dust extinction (which is small at intermediate and high Galactic latitudes). Similar AME/synchrotron results are obtained when using the H\$\alpha\$ map of Finkbeiner (2003) but with small (but significant) differences for the free–free component. As discussed earlier, the stronger correlation of microwave data with the D03 map suggests this version of the map is a better tracer of free–free emission. This will be discussed further in Section 5.2. Although the free–free emission is a small fraction of the total emission at 4.7 GHz, we subtract a model of free–free emission based on the D03 H\$\alpha\$ template, scaled with a value of 0.32 mK R\$^{-1}\$ appropriate for this frequency (Dickinson et al. 2003). This has minimal impact on the results.

For the dust-correlated component we use a range of dust templates listed in Table 2. We quote the results for the best-fitting dust template, the *Planck* thermal dust optical depth map at 353 GHz, τ_{353} , although similar (but not identical) results are found with the rest. Fig. 5 shows the 22.8 GHz map alongside

⁷Template coefficient units are typically brightness (e.g. μ K) per unit template (e.g. K or MJy sr⁻¹). In the case of τ_{353} , which is dimensionless, the coefficient is just brightness (K).

2854 C. Dickinson et al.

Table 3. CC template fitting results for $\delta_{lim} > +80^{\circ}$. Each entry is a correlation coefficient in units given in the second column. The two halves of the table are for when the Haslam 408 MHz (*top*) and C-BASS 4.7 GHz (*bottom*) maps are used as the synchrotron template. CMB fluctuations have been removed by direct subtraction of the *Planck* SMICA map. Uncertainties do not include absolute calibration errors.

Template	Unit	WMAP 22.8 GHz	Planck 28.4 GHz	WMAP 33.0 GHz	WMAP 40.7 GHz	Planck 44.1 GHz
Synchrotron (Haslam) H α (D03) Dust (τ_{353})	μΚ Κ ⁻¹ μΚ R ⁻¹ Κ	9.19 ± 0.39 10.2 ± 1.9 9.93 ± 0.35	5.22 ± 0.27 5.66 ± 1.6 4.77 ± 0.21	3.19 ± 0.25 5.09 ± 1.6 3.11 ± 0.18	$1.70 \pm 0.23 2.83 \pm 1.6 1.57 \pm 0.16$	$ \begin{array}{r} 1.54 \pm 0.22 \\ 3.84 \pm 1.5 \\ 1.11 \pm 0.15 \end{array} $
Synchrotron (C-BASS) Hα (D03) Dust (τ ₃₅₃)	μΚ mK ⁻¹ μΚ R ⁻¹ Κ	10.1 ± 0.41 13.1 ± 1.9 9.52 ± 0.34	5.64 ± 0.29 7.30 ± 1.6 4.56 ± 0.21	3.48 ± 0.26 6.12 ± 1.6 2.98 ± 0.18	1.80 ± 0.24 3.36 ± 1.6 1.51 ± 0.16	$ \begin{array}{c} 1.67 \pm 0.23 \\ 4.33 \pm 1.5 \\ 1.05 \pm 0.15 \end{array} $

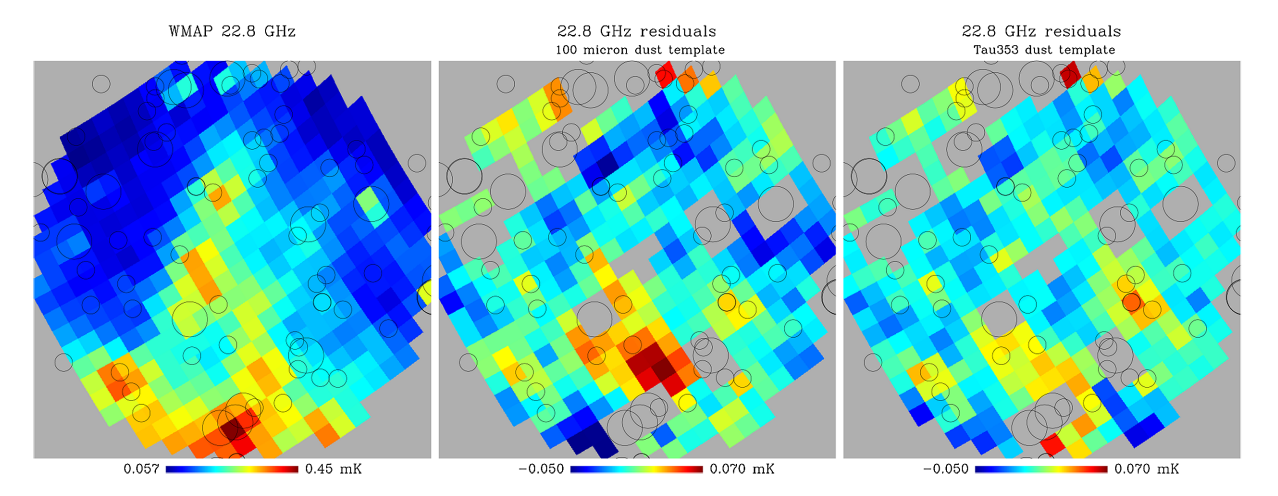


Figure 5. WMAP 22.8 GHz map (left) and residual maps at 22.8 GHz after template fitting when using the 100 μm dust template (middle) and the τ_{353} dust template (right). Maps are at 1° FWHM angular resolution and $N_{\text{side}} = 64$. The coordinate system is the same as in Fig. 3. The colour scales are linear but cover reduced temperature scale (by a factor of ≈7) in the residual maps, shown by the minimum/maximum values to the side of the colour bar. There are larger dust-correlated residuals remaining when using the 100 μm compared to the τ_{353} as a tracer of dust.

residual maps after template fitting, when using the 100 μ m and τ_{353} maps as dust templates. One can clearly see significant residuals when using the 100 μ m map. These will be discussed further in Section 5.3. For the best-fitting templates, the residual 22.8 GHz map after subtraction of the sky components has an rms of 15 μ K (21 μ K when using the 100 μ m dust template), which is comparable to the noise level in this region of 5–10 μ K rms; no obvious large-scale emission is evident. The residuals are mostly due to small contribution (\sim 5 per cent rms compared to the total rms in the map) from extragalactic sources that have not been masked. This is reflected in the χ^2_r values, but has been shown to have little impact on the results when trying different flux level cuts (Section 4.2).

We fit for an offset term since the zero levels, particularly in the low-frequency radio data, are not well determined (the WMAP/Planck data have had a correction for the monopole term, but residual monopoles will exist at some level). This term accounts for this difference and means that the C-BASS zero-level is irrelevant. We also tried fitting for a two-dimensional plane across the field to account for the large-scale Galactic gradient across the field, which could potentially dominate the correlation. We found that the results with or without this term were consistent within the uncertainties. This suggests that either the large-scale emission is not dominant, or it has a spectrum similar to that in the middle of the NCP field.

The results, and in particular the variations of the three components with different templates and assumptions, will be discussed further in Section 5.

4.4 Foreground SEDs

We can convert the template coefficients derived in Section 4.3 for each template-correlated foreground into real units (e.g. μK rms) for each *WMAP/Planck* map that has been fitted to. This is achieved by multiplying the rms in each template (in the natural units of the template) by the corresponding template coefficients (μK per template unit), to give the absolute value of rms fluctuations (in μK , Rayleigh–Jeans) for this particular region of sky and angular resolution. These values can then be used to form a spectral energy distribution (SED) for each component.

Fig. 6 shows the SEDs for the three template-correlated foreground components fitted for all of the *WMAP* and *Planck* channels for $\delta > +80^{\circ}$, based on the results given in Table 3. Filled and open circles are for results using 0.408 and 4.7 GHz, respectively, as the synchrotron template.

It can be seen that the dust-correlated emission dominates the spectrum at all frequencies. At high frequencies ($\gtrsim 80\,\mathrm{GHz}$) the dust-correlated component is due to the low-frequency tail of thermal dust emission while at lower frequencies ($\lesssim 50\,\mathrm{GHz}$) it is due to AME. The 100/217 GHz *Planck* data points are artificially

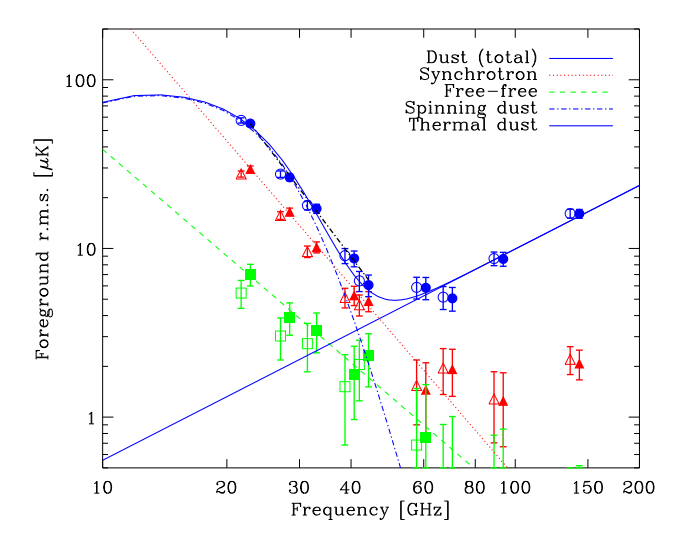


Figure 6. SEDs of the three template-correlated foreground components in the NCP ($\delta > +80^{\circ}$) region: dust (*blue circles*), synchrotron (*red triangles*), and free–free (*green squares*). Filled symbols are when the C-BASS 4.7 GHz map is used as a synchrotron template, while unfilled is when the Haslam 408 MHz map is used; the data points have been shifted slightly to the left for clarity. Coloured straight lines are power-law fits to each component of emission. The *black dot–dashed* line is a power-law fit to the dust-correlated coefficients between 22.8 and 44.1 GHz and the fits were made to the filled circle data points. All data points were evaluated after direct subtraction of the CMB anisotropies using the *Planck* SMICA map.

high because of the contribution of CO lines in the *Planck* data (Planck Collaboration XIII 2014b) and have not been plotted. The synchrotron emission is significant and has a steep ($\beta \approx -3.0$) spectrum while free–free emission is the weakest. One of the major results of this work is that the dust-correlated (AME) emission at 20–40 GHz is not substantially changed when using the higher frequency C-BASS 4.7 GHz map instead of the Haslam 408 MHz map. The C-BASS data constrain the synchrotron emission to be about half of the dust-correlated emission at frequencies \sim 20–40 GHz. However, it is interesting to see that the synchrotron emission appears to be slightly brighter at 20–40 GHz when using the C-BASS map as the synchrotron template. This will be discussed further in Section 5.

5 DISCUSSION

We now discuss in turn the fitted components, beginning with the synchrotron and free-free components, followed by the dust-correlated (AME) component at \sim 20–40 GHz. Unless otherwise stated, quoted results are from the template fitting results presented in Section 4.3, for the Haslam and C-BASS templates. In this section, we will also include specific results from additional analyses.

5.1 Synchrotron emission

From inspection of the synchrotron templates it appears that synchrotron emission is not dominant in the NCP region at frequencies $\sim\!\!20\text{--}40\,\text{GHz}.$ Nevertheless, using the CC technique we are able to detect synchrotron fluctuations with high significance, particularly at frequencies below $\sim\!\!40\,\text{GHz}.$ Synchrotron emission accounts for $29.6\pm1.2\,\mu\text{K}$ rms at $22.8\,\text{GHz},$ which is $\approx\!\!33$ per cent of the total emission at $22.8\,\text{GHz}$ (see Fig. 6). The spectral fit suggests that synchrotron emission becomes dominant below $\approx\!\!15\,\text{GHz}.$

Table 4. Derived synchrotron spectral indices over various frequency ranges and methods. The methods used are T–T plots (TT), template correlation coefficients (CC), and power-law fitting of the derived spectrum (PL). The uncertainties include absolute calibration uncertainties.

Method	Synchrotron spectral index β
TT	-2.79 ± 0.17
CC	-2.85 ± 0.05
CC	-2.88 ± 0.03
CC	-2.91 ± 0.04
PL	-2.85 ± 0.14
	TT CC CC CC

An important result of this analysis is that the amplitude and spectrum of synchrotron emission is consistent when using either the Haslam or C-BASS maps as a template, resulting in little change in the separated AME component. However, the synchrotron amplitudes are consistently ≈ 10 per cent higher when the C-BASS map is used. This could be due to the fact that the higher frequency is detecting more emission with a flatter spectral index, or, that the improved fidelity of the C-BASS map gives a better correlation with the data. It cannot be due to contamination by free-free emission because this is negligible at 408 MHz, while at 4.7 GHz we subtract the small contribution of free–free emission using the H α template. The fact that the goodness-of-fit is better when using C-BASS $(\chi_r^2 = 1.54)$ compared to Haslam $(\chi_r^2 = 2.04)$ suggests that the C-BASS data traces the sky fluctuations better than the Haslam map; the residual rms at 22.8 GHz goes from 17.6 to 15.3 µK. The bestfitting power law to the synchrotron coefficients below 44.1 GHz for the C-BASS template (shown as a red dotted line in Fig. 6) yields $\beta = -2.85 \pm 0.14$.

The template coefficients can be converted directly to a spectral index from the template frequency (e.g. 408 MHz or 4.7 GHz) to the frequency of the data being fitted to (e.g. WMAP/Planck). For a power law, $T \propto v^{\beta}$, the spectral index between two frequencies v_1 and v_2 is given by $\beta = \log(\Delta T_1/\Delta T_2)/\log(v_1/v_2)$. The template coefficient is effectively the ratio of variations in temperatures, ΔT_1 and ΔT_2 . Table 4 summarizes the main synchrotron spectral index measurements from our analyses. It can be seen that consistent values are obtained over the entire frequency range and using different methods. The spectral slope at 20-40 GHz is consistent with the spectral indices derived solely from the radio data as well as the coefficients directly, suggesting that a power law with $\beta = -2.9$ is a good approximation for synchrotron emission from ~1 GHz up to tens of GHz in this region of the sky. Although not formally significant in the NCP region, there is a hint of steepening with frequency, consistent with earlier results (e.g. Davies et al. 2006; Strong et al. 2011; Kogut 2012). This is in contrast to Peel et al. (2012) who found a hint of flattening from 23 to 41 GHz ($\Delta \beta \approx$ 0.05), but again, at the $\sim 1\sigma$ significance level.

One caveat to this simple picture is that when considering only the inner regions of the map at the highest declinations, the synchrotron spectrum appears to flatten slightly. For the case of $\delta>+83^\circ,$ although the other coefficients are consistent to better than $2\sigma,$ the C-BASS synchrotron coefficient at 22.8 GHz increases to $13.6\pm0.8\,\mu\text{K mK}^{-1},$ corresponding to a synchrotron spectral index of $\beta=-2.72\pm0.05.$ The other components do not change as significantly because the dust-correlated emission dominates the fluctuations at 23 GHz. This suggests that the synchrotron emission in and around the two main AME dust clouds and NCP is slightly flatter than the large-scale emission from the Galactic plane. Nevertheless, the synchrotron emission remains a small component relative to the

Table 5. Fluctuations of rms at 22.8 GHz of each component for $\delta > +80^{\circ}$ from the CC analysis and from the *Planck* 2015 COMMANDER component separation products (Planck Collaboration X 2016a). Units are μ K.

Component	CC	Planck 2015	
Synchrotron	29.6 ± 1.2	11.8	
Free-free	7.0 ± 1.0	46.9	
AME/dust	55.0 ± 2.0	45.4	
Thermal dust	_	1.2	
Total foreground	88.8 ± 3.6	84.0	

total emission at 22.8 GHz. The equivalent spectral index from 0.4 to 22.8 GHz remains consistent between the two sky areas, so if the flattening is real it is occurring above a frequency of a few GHz and then steepening again at higher frequencies (otherwise we would see flatter indices above 4.7 GHz).

An important consideration for the interpretation of synchrotron emission is the presence of free-free emission in the low-frequency radio data. At high Galactic latitudes, the H α intensities are typically a few R at most. The H α map of the NCP region (Fig. 3) shows emission at a level of ~1 R with a peak of 3.7 R on a background of \approx 0.5–1 R; see Section 5.2. A typical high-latitude H α intensity of 1 R corresponds to 51 mK at 408 MHz and 0.3 mK at 4.7 GHz (Dickinson et al. 2003). Therefore the contribution from free-free at high latitudes is negligible at 408 MHz (typical fluctuations of \sim 10 K) and a small contribution at 4.7 GHz (typical fluctuations \approx 5 mK). Even though it had little impact on the quoted results, we subtracted the free-free contribution at 4.7 GHz using the H α map and a conversion factor of 0.32 mK R⁻¹. As a further test, we performed template-fitting of the C-BASS map itself, using the $408\,\mathrm{MHz}$ and $\mathrm{H}\,\alpha$ maps as tracers of the synchrotron and free-free emission, respectively. We do not detect H α -correlated emission in the NCP region at 4.7 GHz, with a template coefficient of 0.29 ± 0.31 mK R⁻¹, which is consistent with theoretical expectations. Virtually all of the signal at 4.7 GHz can be accounted for by the 408 MHz template, with a coefficient of 935 \pm 72 mK K⁻¹, corresponding to $\beta = -2.85 \pm 0.05$. This can be contrasted with emission from the Galactic disc, which emits a much larger fraction of free-free emission at 4.7 GHz (Irfan et al. 2015).

Table 5 lists the rms values for each component from the CC analysis for $\delta > +80^{\circ}$, calculated by multiplying the CC template coefficients by the rms fluctuations in the template map for this region. Taking into account correlations between the templates gives a total rms of 89.4 \pm 4.1 μ K at 22.8 GHz. We also list the rms values from the corresponding Planck 2015 COMMANDER component separation products (Planck Collaboration X 2016a), scaled to 22.8 GHz. We can see that in the CC analysis using C-BASS, although the AME dominates the fluctuations, the synchrotron emission contributes almost three times more rms fluctuations compared to the *Planck* COMMANDER solution. This is due to the fact that the *Planck* COMMANDER analysis used only one low-frequency data point at 408 MHz, which meant that the synchrotron spectrum had to be effectively fixed. Their model had an effective spectral index of $\beta \approx -3.05 \pm 0.05$ above 1 GHz (Planck Collaboration XXV 2016c), while the C-BASS data prefers a slightly flatter index of $\beta \approx -2.9$.

Finally, we comment on the apparent upturn in the synchrotron spectrum above $\sim\!90\,\mathrm{GHz}$ (Fig. 6). At these frequencies the synchrotron component accounts for $\ll 10$ per cent of the total emission and therefore is difficult to separate from the much brighter dust emission and is also partially (spatially) correlated. This is

partially reflected in the larger error bars and therefore we do not believe the upturn to be a real effect.

5.2 Free-free emission

The $H\alpha$ -correlated component is expected to be due to free-free emission (Dickinson et al. 2003). For an electron temperature $T_{\rm e} =$ $8000 \,\mathrm{K}$, typical of the diffuse ISM, we would expect to see H α template coefficients of 11.4, 7.8, 5.23, 3.28, and 1.11 μ K R⁻¹, for frequencies of 22.8, 28.4, 33.0, 40.7, 44.1 GHz, respectively. It also assumes that the correction for dust extinction along the line of sight has been done accurately, which renders the standard H α templates useless at very low Galactic latitudes (Dickinson et al. 2003). The theoretical values also assume local thermodynamic equilibrium, 8 per cent contribution from helium, and that there is no scattering of H α from elsewhere off dust grains. The amount of scattered H α light is not clear, with earlier predictions in the range 5-20 per cent (Wood & Reynolds 1999), while more recent work has suggested that it could be more significant along some lines of sight (Brandt & Draine 2012; Seon & Witt 2012) and possibly up to 50 per cent or more (Witt et al. 2010). This would in turn reduce these coefficients by up to a half, giving better agreement with theory (Banday et al. 2003; Davies et al. 2006; Dobler, Draine & Finkbeiner 2009; Ghosh et al. 2012).

From our analysis, the free-free emission is very weak in the NCP region. The free-free brightness has an rms of $7.0 \pm 1.0 \,\mu\text{K}$ at 22.8 GHz (Table 5), corresponding to ≈6 per cent of the total emission. Nevertheless, the H α -correlated values in Table 3 are consistent with theoretical expectations; at 22.8 GHz we expect $\approx 11 \,\mu K \, R^{-1}$ for typical electron temperatures (Dickinson et al. 2003). Moreover, while the uncertainties are relatively large, the independent coefficients plotted in Fig. 6 precisely follow the spectral dependence expected for free–free emission ($\beta \approx -2.1$) up to 44 GHz and higher. This is good reassurance that the template fits are yielding physically meaningful results. A previous analysis of the H α fluctuations in the NCP region ($\delta > +81^{\circ}$) by Gaustad, McCullough & van Buren (1996) found an upper limit of 0.5 R on 1° scales, corresponding to < 6 μK at 22.8 GHz. This is consistent with our analysis at the 1σ level. We note that the *Planck* 2015 freefree map gives a much larger rms amplitude of 46.9 µK (Table 5), at the expense of both the AME and synchrotron components. This is the largest discrepancy between the two analyses. As discussed and demonstrated by Planck Collaboration XXV (2016c), the COMMANDER free-free solution appears to be overestimated (typically by a factor of several) due to aliasing of the low-frequency (synchrotron or free-free or AME) components by the spectrum alone.

The H α coefficients from our analysis are consistent with expectations from theory, for electron temperatures in the range $T_{\rm e} \approx 7000$ –10 000 K; this indicates that scattered H α is not a major issue in this region of sky. They are also consistent when using either of the synchrotron templates. Note that we chose to subtract the free–free component from the C-BASS 4.7 GHz map to ensure it was dominated by synchrotron emission. When using the raw 4.7 GHz without a free–free correction, we naturally found a lower value for the template coefficient of 9.9 \pm 1.9 μ K R $^{-1}$ at 22.8 GHz, indicating that residual free–free emission in the 4.7 GHz map is having a small impact, at least on the free–free solution. Fortunately, it has negligible impact on the other template results, with the values changing by less than 0.2 σ for both the synchrotron- and dust-correlated coefficients. This highlights that the free–free emission is relatively weak at all microwave frequencies.

The two H α templates (F03 and D03) also give slightly different results (but consistent within the uncertainties), which can be attributed largely to stellar residuals in the H α maps that have been treated differently. The H α -correlated template coefficient at 22.8 GHz when using F03 was $18.2 \pm 2.9 \,\mu\text{K}\,\text{R}^{-1}$, slightly higher than for D03, which is expected due to the small fluctuations in the F03 version of the map. This also had a minor impact on the synchrotron and dust coefficients but is consistent to within 1.5σ . The dust reddening E(B-V) map of Schlegel, Finkbeiner & Davis (1998) can be used to estimate the maximum level of dust extinction assuming all the dust is in front of the ionized gas (Dickinson et al. 2003). At the original 6.1 arcmin resolution, the main dust feature in this region has extinction values in the range $\approx 0.2-0.7$ mag; at 1° resolution the two dust emission peaks are at a value of ≈ 0.45 mag, corresponding to a maximum dust absorbing factor of ≈ 1.5 . It is therefore possible that the H α intensity is underestimated in this region by \approx 20-30 per cent (about half of the maximum value). This would not have a significant effect on the synchrotron and AME results because the free-free component is sub-dominant, being ≈ 7 per cent of the total emission.

In summary, the D03 H α template appears to trace free-free emission more reliably than the F03 map, with an amplitude that is as expected for typical electron temperatures of $T_{\rm e} \approx 7000$ –10 000 K. The free-free emission at AME frequencies (\approx 20–40 GHz) in the NCP region appears to be a small portion of the total emission, and therefore assumptions about the template and dust extinction have little effect on the AME amplitude.

5.3 AME

Our results show a significant detection of dust-correlated emission, particularly in the $\sim\!20\text{--}40$ GHz range. The dust-correlated emission (AME) is much brighter than can be accounted for by thermal dust (which would have a falling spectrum with decreasing frequency) and synchrotron/free–free emission as traced by the foreground templates. The rms of the dust-correlated component at 22.8 GHz is $55.0\pm2.0\,\mu\text{K}$ at 22.8 GHz, which accounts for $\approx\!60$ per cent of the total rms (Table 5).

The main result of this paper is the lack of change in the AME signal relative to the FIR data, when using the higher frequency C-BASS 4.7 GHz template compared to the traditional Haslam 408 MHz map. This is a similar result to those previously found when using a 2.3 GHz map as a synchrotron template (Peel et al. 2012), who found the AME amplitude changed by only 7 per cent. For our baseline fit, when using the τ_{353} map as the dust template, we find coefficients at 22.8 GHz of 9.93 \pm 0.35 K and 9.52 \pm 0.34 K per unit τ_{353} (Table 3), when using the Haslam and C-BASS maps as synchrotron templates, respectively, i.e. they are consistent at the \approx 1 σ level with just a 4 per cent change in amplitude.

Our main result is consistent with the spectral indices for synchrotron emission that are almost constant across the entire radio/microwave band (see Section 5.1). An additional flatter (harder) spectrum component of synchrotron is not detected at 4.7 GHz. For synchrotron emission to explain the bulk of the AME, it would have to have a much flatter spectrum; a value of $\beta \approx -2.3$ would be needed to extrapolate the ~ 3 mK rms fluctuations at 4.7 GHz to the ~ 80 µK fluctuations observed at 22.8 GHz (after removing the CMB and free–free contribution). However, in practice it would need to be even flatter than this, since the observed emission at 4.7 GHz does not correlate well with the AME, and hence a flat synchrotron AME component would need to be subdominant at 4.7 GHz.

Table 6. AME CC template coefficients at 22.8 GHz and χ_r^2 values for different dust templates, ordered in terms of decreasing goodness-of-fit.

Template	Correlation Coeff.	Unit	χ_r^2
$ au_{353}$	9.52 ± 0.34	K	1.54
Planck 545 GHz	67 ± 2	$\mu \text{K} (\text{MJy sr}^{-1})^{-1}$	1.60
FDS94	5.16 ± 0.19	$mK mK^{-1}$	1.62
Planck 857 GHz	22.4 ± 0.8	$\mu \text{K} (\text{MJy sr}^{-1})^{-1}$	1.63
Planck 353 GHz	875 ± 32	$\mu \text{K mK}^{-1}$	1.63
Dust radiance R	563 ± 20	$K(W m^{-2} sr^{-1})^{-1}$	2.12
IRIS 100 μm	31.0 ± 1.1	$\mu\mathrm{K}(\mathrm{MJy}\mathrm{sr}^{-1})^{-1}$	2.90

We find similar levels of AME in the NCP region, relative to the standard dust templates, to those measured previously. Table 6 lists the AME CC template coefficients at 22.8 GHz and χ_r^2 values for each dust template. We adopt τ_{353} as our default template since it formally provided the best fit to the microwave data, with map residuals of 15 µK rms. Our best value of 9.52 ± 0.34 K compares well with the high-latitude ($|b| > 10^\circ$) value of 9.7 ± 1.0 K (Planck Collaboration XXV 2016c). Hensley et al. (2016) found a value of 7.9 ± 2.6 K at 30 GHz, which is also consistent. We find slightly larger fluctuations in the AME at 22.8 GHz (55 ± 2 µK) compared to the *Planck* products (45.4 µK), but they are comparable (Table 5). This shows that even with very different component separation techniques, the AME is a strong component of the emission at frequencies ≈ 20 –40 GHz.

We tried several other standard dust templates, listed in Tables 2 and 6. The worst template is the 100 µm template, which is confirmed by the Pearson correlation coefficients at 22.8 GHz (where AME is dominant), as shown in Section 3.3. It is also evident in the residual maps at 22.8 GHz presented in Fig. 5; the residual map rms at 22.8 GHz increases from 15 μK to 21 μK rms. This is presumably due to variations in the dust composition or temperature, which significantly modulates the response at wavelengths near the peak of the spectrum at \sim 100 μ m but has negligible effect at longer wavelengths (e.g. Finkbeiner 2004; Tibbs, Paladini & Dickinson 2012). Nevertheless, we measured coupling coefficients of 31.0 \pm $1.1 \,\mu\text{K} \,(\text{MJy sr}^{-1})^{-1}$ at 22.8 GHz and $9.9 \pm 0.7 \,\mu\text{K} \,(\text{MJy sr}^{-1})^{-1}$ at 33.0 GHz. This compares well with the $\approx 10 \,\mu\text{K} \,(\text{MJy sr}^{-1})^{-1}$ at 33.0 GHz that has been observed before (Banday et al. 2003; de Oliveira-Costa et al. 2004; Davies et al. 2006). This can also be compared with the dust-correlation measured originally by Leitch et al. (1997), which when extrapolated to 22.8 GHz, corresponds to 77 μ K (MJy sr⁻¹)⁻¹. This value is higher because it is a direct (single template) correlation, therefore neglecting any dustcorrelated synchrotron/free-free emission. Also, their best-fitting spectral index of -2.2 is flatter than most measurements since then, which increases the relative amplitude at higher frequencies. The interpretation is that about half of the total dust-correlated signal at 20-40 GHz is due to AME.

Interestingly, unlike the results of Hensley et al. (2016) the map of dust radiance (\Re) was found not to trace AME as well as τ_{353} or any of the *Planck* HFI maps. Nevertheless, we found similar amplitudes to those estimated at high latitudes. For example, for the case of the dust radiance template, we found a coefficient of $563 \pm 20 \text{ K (W m}^{-2} \text{ sr}^{-1})^{-1}$ compared to $226 \pm 44 \text{ K (W m}^{-2} \text{ sr}^{-1})^{-1}$ at 30 GHz. Surprisingly, the much older FDS94 model (Finkbeiner et al. 1999) provided almost as good a fit as τ_{353} . Our coefficient of $5.16 \pm 0.19 \text{ mK mK}^{-1}$ is slightly lower than the equivalent region 6 of Davies et al. (2006) who found $6.7 \pm 0.7 \text{ mK mK}^{-1}$. When adopting the Haslam synchrotron template we obtained a consistent

value of $5.38 \pm 0.19 \, \text{mK} \, \text{mK}^{-1}$. The slight difference is mostly due to the slightly different sky areas and masking used.

From Fig. 6 it is clear that using the much higher frequency synchrotron template from C-BASS makes little difference to the dust-correlated (AME) component, at least in this region of the sky. This indicates that there is no strong component of flatspectrum synchrotron emission. The spectrum of the dust-correlated component also appears to be well approximated at \sim 20–40 GHz by a power law with a best-fitting slope of $\beta = -3.23 \pm 0.13$, which is slightly steeper but remarkably close to the spectrum of the synchrotron component ($\beta \approx -2.9$). We fitted a spinning dust model, using the SPDUST2 code (Ali-Haïmoud, Hirata & Dickinson 2009; Silsbee, Ali-Haïmoud & Hirata 2011), adopting the parameters for the cold neutral medium (CNM) as suggested by Draine & Lazarian (1998a). This gave a poor fit because this particular model spectrum peaks at 33 GHz (in flux density units). We therefore included a frequency shift (in log space) of the CNM spinning dust spectrum, which provided a good fit with a peak frequency of 23 GHz, as shown in Fig. 6. However, there is an indication that there is excess emission in the range \approx 50-100 GHz. This is likely a failure of the simple single-component CNM spinning dust model.

In reality, there will be a range of dust particles/environments along the line of sight that will tend to broaden the spectrum, and which motivated the two-component model by Planck Collaboration X, IV (2016a,c). Note that spinning dust models generally predict broadly peaked emission spectra with a FWHM in frequency approximately twice the peak frequency; for e.g. the WNM model of Draine & Lazarian (1998b) has a peak at 22 GHz in flux density, with half-max points at 13 and 37 GHz. The location of the peak is determined by a combination of the nanoparticle size distribution, the electric dipole moment, and the excitation conditions.

Using a single-component model results in a thermal dust emissivity index of $\beta=+1.25\pm0.13$, which is significantly flatter than has been measured for the majority of the sky with $\beta\approx1.6$ (e.g. Planck Collaboration XI 2014a). The low value is within the range measured by *Planck* but is sensitive to which CMB map is used and over which frequencies are being fitted. It does not change the results for AME, which dominates at lower frequencies where the thermal dust has a minimal contribution. Given the lack of alternatives, the spinning dust mechanism appears to be the most viable explanation for the diffuse AME observed in the NCP region.

6 CONCLUSIONS

We have re-analysed the NCP region ($\delta > +80^{\circ}$) in WMAP/Planck data to study the diffuse foregrounds. We used template maps of synchrotron (low-frequency radio maps), free–free (H α maps) and dust emission (sub-mm/FIR maps) to fit to WMAP/Planck data at 22.8 GHz and above. In addition to the standard Haslam 408 MHz map, we used new C-BASS data at 4.7 GHz as a tracer of synchrotron emission. C-BASS data are of higher quality than the Haslam et al. (1982) data, which are known to contain significant striations and other calibration issues. More importantly, at a frequency of \approx 4.7 GHz, C-BASS data are much closer to the frequencies observed by WMAP/Planck and therefore should be more representative of foregrounds at microwave frequencies. In particular, if there is a significant hard (flat spectrum) component of synchrotron radiation, then the C-BASS maps should be a more reliable synchrotron template.

We have found that the dust-correlated AME component accounts for the bulk (\approx 60 per cent) of the foreground rms in the NCP region and that it does not change significantly when including the C-BASS 4.7 GHz map. The synchrotron emission has a spectrum close to $\beta =$ -2.90 ± 0.05 when considering the low-frequency data alone via T-T plots, the CC coefficients directly, or when fitting to the SED of coefficients in the range 20-40 GHz. This indicates that a power law is a good model for the synchrotron emission from a frequency of 0.4 GHz up to tens of GHz and that there is no strong component of flat-spectrum (harder) synchrotron emission, at least in the NCP region. The synchrotron component accounts for approximately half the rms brightness at 22.8 GHz. We find that the D03 version of the H α map correlates better with microwave data than the F03 map, due to low level residual artefacts in the maps. Fortunately, free-free emission is relatively weak at high latitudes and accounts for \approx 6 per cent of the total signal at 22.8 GHz.

We preferred the thermal dust optical depth at 353 GHz as our tracer of AME since it gave the best overall fit. We found a best-fitting template coefficient of 9.52 \pm 0.34 K per unit τ_{353} at 22.8 GHz, which agrees well with previous measurements on different regions of the sky. Other templates, such as dust radiance and FDS94 gave similar results but with slightly larger residuals. The most discrepant of the dust tracers was the IRIS 100 μm map, due to variations in dust temperature within the region, which modulates the spatial morphology at wavelengths near $100\,\mu m$

A power law provides a good fit to the AME spectrum above 20 GHz. Alternatively, it can be well-fitted by a shifted spinning dust model, with a peak frequency (flux density units) around 23 GHz. However, in this case the thermal dust emissivity index flattens to $\approx + 1.3$. This is likely a failure of a simple single-component spinning dust model, which is inevitably narrower than the true distribution of dust particles and environments.

The observations for the northern C-BASS survey are now complete and the southern survey is just beginning. With full-sky C-BASS maps we will be able to investigate the AME across the whole sky and to investigate the possible contribution of a harder spectrum of synchrotron radiation. Future papers will include applying T-T plot (Jew et al., in preparation) and template fitting (Harper et al., in preparation) techniques to the high-latitude sky. We will also use more advanced component separation techniques such as parametric fitting (e.g. Eriksen et al. 2008). With the wealth of high-precision data covering a wide range of frequencies, including new data from S-PASS (Krachmalnicoff et al. 2018) and QUIJOTE (Génova-Santos et al. 2015), we should be able to fit for all these components as a function of position on the sky.

ACKNOWLEDGEMENTS

The C-BASS project is a collaboration between Oxford and Manchester Universities in the UK, the California Institute of Technology in the U.S.A., Rhodes University, UKZN and the South African Radio Observatory in South Africa, and the King Abdulaziz City for Science and Technology (KACST) in Saudi Arabia. It has been supported by the National Science Foundation NSF awards AST-0607857, AST-1010024, AST-1212217, and AST-1616227, and NASA award NNX15AF06G, the University of Oxford, the Royal Society, the Science and Technology Facilities Council (STFC), and the other participating institutions. This research was also supported by the South African Radio Astronomy Observatory, which is a facility of the National Research Foundation, an agency

of the Department of Science and Technology. We would like to thank Russ Keeney for technical help at the Owens Valley Radio Observatory. CD acknowledges support from a European Research Council ERC Starting (Consolidator) Grant (no. 307209). CD also thanks the California Institute of Technology for their hospitality and hosting during several extended visits. MWP acknowledges funding from a FAPESP Young Investigator fellowship, grant 2015/19936-1. We make use of the HEALPIX package (Górski et al. 2005), IDL astronomy library and PYTHON astropy, matplotlib, numpy, healpy, and scipy packages. This research has made use of the NASA/IPAC Extragalactic Database (NED) which is operated by the Jet Propulsion Laboratory, California Institute of Technology, under contract with the National Aeronautics and Space Administration. The C-BASS collaboration would like to remember the late Prof. Rodney D. Davies and Prof. Richard J. Davis, who were both strong supporters of the C-BASS project (http://cbass.web.ox.ac.uk).

REFERENCES

Ali-Haïmoud Y., Hirata C. M., Dickinson C., 2009, MNRAS, 395, 1055
Alves M. I. R., Davies R. D., Dickinson C., Calabretta M., Davis R., Staveley-Smith L., 2012, MNRAS, 422, 2429

AMI Consortium et al., 2011, MNRAS, 415, 2708

Armitage-Caplan C., Dunkley J., Eriksen H. K., Dickinson C., 2012, MNRAS, 424, 1914

Banday A. J., Dickinson C., Davies R. D., Davis R. J., Górski K. M., 2003, MNRAS, 345, 897

Bennett C. L. et al., 2003, ApJS, 148, 97

Bennett C. L. et al., 2013, ApJS, 208, 20

Brandt T. D., Draine B. T., 2012, ApJ, 744, 129

Casassus S., Cabrera G. F., Förster F., Pearson T. J., Readhead A. C. S., Dickinson C., 2006, ApJ, 639, 951

Casassus S. et al., 2008, MNRAS, 391, 1075

Condon J. J., Cotton W. D., Greisen E. W., Yin Q. F., Perley R. A., Taylor G. B., Broderick J. J., 1998, AJ, 115, 1693

Davies R. D., Watson R. A., Gutierrez C. M., 1996, MNRAS, 278, 925

Davies R. D., Dickinson C., Banday A. J., Jaffe T. R., Górski K. M., Davis R. J., 2006, MNRAS, 370, 1125

de Oliveira-Costa A., Tegmark M., Davies R. D., Gutiérrez C. M., Lasenby A. N., Rebolo R., Watson R. A., 2004, ApJ, 606, L89

de Zotti G., Massardi M., Negrello M., Wall J., 2010, A&AR, 18, 1

Delabrouille J., Cardoso J., 2009, in Martínez V. J., Saar E., Martínez-González E., Pons-Bordería M.-J., eds, Lecture Notes in Physics, Vol. 665, Data Analysis in Cosmology. Springer-Verlag, Berlin, p. 159

Dickinson C., Davies R. D., Davis R. J., 2003, MNRAS, 341, 369

Dickinson C. et al., 2009, ApJ, 690, 1585

Dickinson C. et al., 2010, MNRAS, 407, 2223

Dickinson C., Peel M., Vidal M., 2011, MNRAS, 418, L35

Dickinson C. et al., 2018, New Astron. Rev., 80, 1

Dobler G., Draine B., Finkbeiner D. P., 2009, ApJ, 699, 1374

Draine B. T., Lazarian A., 1998a, ApJ, 494, L19

Draine B. T., Lazarian A., 1998b, ApJ, 508, 157

Draine B. T., Lazarian A., 1999, ApJ, 512, 740

Draine B. T., Hensley B., 2013, ApJ, 765, 159

Dunkley J. et al., 2009a, in Dodelson S. et al., eds, AIP Conf. Proc. Vol. 1141, Prospects for Polarized Foreground Removal. Am. Inst. Phys., New York, p. 222

Dunkley J. et al., 2009b, ApJ, 701, 1804

Erickson W. C., 1957, ApJ, 126, 480

Eriksen H. K., Jewell J. B., Dickinson C., Banday A. J., Górski K. M., Lawrence C. R., 2008, ApJ, 676, 10

Errard J., Stompor R., 2012, Phys. Rev. D, 85, 083006

Finkbeiner D. P., 2003, ApJS, 146, 407

Finkbeiner D. P., 2004, ApJ, 614, 186

Finkbeiner D. P., Davis M., Schlegel D. J., 1999, ApJ, 524, 867

Finkbeiner D. P., Schlegel D. J., Frank C., Heiles C., 2002, ApJ, 566, 898 Gaustad J. E., McCullough P. R., van Buren D., 1996, PASP, 108, 351

Génova-Santos R. et al., 2015, in Cenarro A. J., Figueras F., Hernández-Monteagudo C., Trujillo Bueno J., Valdivielso L., eds, Highlights of Spanish Astrophysics VIII. Spanish Astronomical Society, Teruel, Spain, p. 207

Génova-Santos R. et al., 2017, MNRAS, 464, 4107

Ghosh T., Banday A. J., Jaffe T., Dickinson C., Davies R., Davis R., Gorski K., 2012, MNRAS, 422, 3617

Gold B. et al., 2011, ApJS, 192, 15

Górski K. M., Hivon E., Banday A. J., Wandelt B. D., Hansen F. K., Reinecke M., Bartelmann M., 2005, ApJ, 622, 759

Gregory P. C., Scott W. K., Douglas K., Condon J. J., 1996, ApJS, 103, 427 Haffner L. M., Reynolds R. J., Tufte S. L., Madsen G. J., Jaehnig K. P., Percival J. W., 2003, ApJS, 149, 405

Hargrave P. J., McEllin M., 1975, MNRAS, 173, 37

Haslam C. G. T., Salter C. J., Stoffel H., Wilson W. E., 1982, A&AS, 47, 1
 Healey S. E., Fuhrmann L., Taylor G. B., Romani R. W., Readhead A. C. S., 2009, AJ, 138, 1032

Hensley B. S., Draine B. T., Meisner A. M., 2016, ApJ, 827, 45

Hoang T., Lazarian A., 2016, ApJ, 821, 91

Holler C. M. et al., 2013, IEEE Trans. Antennas Propag., 61, 117

Irfan M. O., 2014, PhD thesis, Univ. Manchester

Irfan M. O. et al., 2015, MNRAS, 448, 3572

Jaffe T. R., Banday A. J., Leahy J. P., Leach S., Strong A. W., 2011, MNRAS, 416, 1152

Jonas J. L., Baart E. E., Nicolson G. D., 1998, MNRAS, 297, 977

Jones M. E. et al., 2018, MNRAS, 480, 3224

King O. G. et al., 2010, in Holland W. S., Zmuidzinas J., eds, SPIE Conf. Ser. Vol. 7741, Millimeter, Submillimeter, and Far-Infrared Detectors and Instrumentation for Astronomy V. SPIE, Bellingham

King O. G. et al., 2014, MNRAS, 438, 2426

Kogut A., 2012, ApJ, 753, 110

Kogut A., Banday A. J., Bennett C. L., Gorski K. M., Hinshaw G., Smoot G. F., Wright E. I., 1996, ApJ, 464, L5

Kogut A. et al., 2007, ApJ, 665, 355

Kogut A. et al., 2011, ApJ, 734, 4

Krachmalnicoff N. et al., 2018, A&A, 618, A166

Kühr H., Pauliny-Toth I. I. K., Witzel A., Schmidt J., 1981a, AJ, 86, 854 Kühr H., Witzel A., Pauliny-Toth I. I. K., Nauber U., 1981b, A&AS, 45, 367 Lagache G., 2003, A&A, 405, 813

Lawson K. D., Mayer C. J., Osborne J. L., Parkinson M. L., 1987, MNRAS, 225, 307

Leach S. M. et al., 2008, A&A, 491, 597

Leitch E. M., Readhead A. C. S., Pearson T. J., Myers S. T., 1997, ApJ, 486,

Liu J., Cui L., Liu X., Ding Z., Song H.-G., 2014, JA&A, 35, 247

López-Caraballo C. H., Rubiño-Martín J. A., Rebolo R., Génova-Santos R., 2011, ApJ, 729, 25

Macellari N., Pierpaoli E., Dickinson C., Vaillancourt J. E., 2011, MNRAS, 418, 888

Markwardt C. B., 2009, in Bohlender D. A., Durand D., Dowler P., eds, ASP Conf. Ser. Vol. 411, Astronomical Data Analysis Software and Systems XVIII. Astron. Soc. Pac., San Francisco, p. 251

Mingaliev M. G., Sotnikova Y. V., Bursov N. N., Kardashev N. S., Larionov M. G., 2007, Astron. Rep., 51, 343

Miville-Deschênes M., Lagache G., 2005, ApJS, 157, 302

Onić D., 2013, Ap&SS, 346, 3

Orlando E., Strong A., 2013, MNRAS, 436, 2127

Peel M. W., Dickinson C., Davies R. D., Banday A. J., Jaffe T. R., Jonas J. L., 2012, MNRAS, 424, 2676

Planck Collaboration XXI, 2011a, A&A, 536, A21

Planck Collaboration XX, 2011b, A&A, 536, A20

Planck Collaboration XII, 2013a, A&A, 557, A53

Planck Collaboration IX, 2013b, A&A, 554, A139

Planck Collaboration XI, 2014a, A&A, 571, A11

Planck Collaboration XII, 2014a, A&A, 571, A11
Planck Collaboration XIII, 2014b, A&A, 571, A13

Planck Collaboration XV, 2014c, A&A, 565, A103

2860 C. Dickinson et al.

Planck Collaboration X, 2016a, A&A, 594, A10

Planck Collaboration IV, 2016b, A&A, 594, A9

Planck Collaboration XXV, 2016c, A&A, 594, A25

Planck Collaboration XXVI, 2016d, A&A, 594, A26

Planck Collaboration XLVIII, 2016e, A&A, 596, A109

Planck Collaboration I, 2018a, A&A, preprint (arXiv:1807.06205)

Planck Collaboration IV, 2018b, A&A, preprint (arXiv:1807.06208)

Platania P., Bensadoun M., Bersanelli M., De Amici G., Kogut A., Levin S., Maino D., Smoot G. F., 1998, ApJ, 505, 473

Reich W., 1982, A&AS, 48, 219

Reich P., Reich W., 1986, A&AS, 63, 205

Reich P., Reich W., 1988, A&AS, 74, 7

Reich P., Testori J. C., Reich W., 2001, A&A, 376, 861

Remazeilles M., Dickinson C., Banday A. J., Bigot-Sazy M.-A., Ghosh T., 2015, MNRAS, 451, 4311

Remazeilles M., Dickinson C., Eriksen H. K. K., Wehus I. K., 2016, MNRAS, 458, 2032

Ricci R. et al., 2013, MNRAS, 435, 2793

Righini S. et al., 2012, MNRAS, 426, 2107

Rubiño-Martín J. A., López-Caraballo C. H., Génova-Santos R., Rebolo R., 2012, Adv. Astron., 2012, 351836

Scaife A. M. M. et al., 2009, MNRAS, 400, 1394

Schlegel D. J., Finkbeiner D. P., Davis M., 1998, ApJ, 500, 525

Seon K.-I., Witt A. N., 2012, ApJ, 758, 109

Silsbee K., Ali-Haïmoud Y., Hirata C. M., 2011, MNRAS, 411, 2750

Strong A. W., Orlando E., Jaffe T. R., 2011, A&A, 534, A54

Sutton D. et al., 2010, MNRAS, 407, 1387

Tibbs C. T. et al., 2011, MNRAS, 418, 1889

Tibbs C. T., Paladini R., Dickinson C., 2012, Adv. Astron., 2012, 124931

Tibbs C. T., Scaife A. M. M., Dickinson C., Paladini R., Davies R. D., Davis R. J., Grainge K. J. B., Watson R. A., 2013, ApJ, 768, 98

Turtle A. J., Pugh J. F., Kenderdine S., Pauliny-Toth I. I. K., 1962, MNRAS, 124, 297

Watson R. A., Rebolo R., Rubiño-Martín J. A., Hildebrandt S., Gutiérrez C. M., Fernández-Cerezo S., Hoyland R. J., Battistelli E. S., 2005, ApJ, 624, L89

Weiland J. L. et al., 2011, ApJS, 192, 19

Williams M. J., Bureau M., Cappellari M., 2010, MNRAS, 409, 1330

Winkel B., Kerp J., Flöer L., Kalberla P. M. W., Ben Bekhti N., Keller R., Lenz D., 2016, A&A, 585, A41

Witt A. N., Gold B., Barnes F. S. III, DeRoo C. T., Vijh U. P., Madsen G. J., 2010, ApJ, 724, 1551

Wood K., Reynolds R. J., 1999, ApJ, 525, 799

This paper has been typeset from a T_EX/IAT_EX file prepared by the author.